Technical University of Munich
Department of Physics

Graduation paper from the Bachelor of Science in Physics

Energy Calibration of the TRISTAN Silicon Drift Detectors

Energiekalibrierung der TRISTAN Siliziumdriftdetektoren

Daniela Spreng
03700307
ge56zay@mytum.de

02 October 2020

Max-Planck-Institute for Physics

Primary reviewer: Prof. Dr. Susanne Mertens
Secondary reviewer: Prof. Dr. Björn Gabrecht
Supervisor: Daniel Benedikt Siegmann

Abstract

Sterile neutrinos are a minimal extension of the Standard Model of elementary particles. They are introduced as the right-handed partners of active neutrinos and, hence, are referred to as 'sterile' as they would not take part in any Standard Model interaction. Their existence would solve several open questions in physics. One of them is the composition of dark matter. Standard Model particles do not provide any suitable candidates that are electrically neutral and stable in respect of the age of the universe. Sterile neutrinos with masses in the keV-scale could be a promising candidate for warm and cold dark matter, though. The TRISTAN project (TRitium Investigation on STerile to Active Neutrino mixing), an expansion of the KATRIN (KArlsruhe TRItium Neutrino) experiment, aims to find sterile neutrinos by analysing the tritium β-decay spectrum. It upgrades the detector section of KATRIN with a multi-pixel Silicon Drift Detector (SDD). Within three years of data taking its goal is to measure the sterile parameter space up to masses of 18.6 keV with a sensitivity of $sin^2(\theta) = 10^{-6}$. For this task the detector has to be able to handle high count rates and have an excellent energy resolution in order to determine the kink-like structure a fourth neutrino mass eigenstate causes on the spectrum.

In addition to a good energy resolution, an excellent energy calibration linearity is a crucial part in understanding the spectrum to find the imprint of a sterile neutrino in the tritium β-decay spectrum. In the scope of this thesis, the accuracy of the energy calibration was investigated with $^{241}_{95}$Am as a mono-energetic photon source. For this, the TRISTAN 7-pixel prototype detector recorded the $^{241}_{95}$Am spectrum for almost ten days. The recorded spectrum was analysed and all peaks were identified. Based on this insight a fitting method was developed in order to precisely determine the peak positions to make the energy calibration as accurate as possible. The impact of charge sharing between two pixels, the energy peak fitting range as well as the energy peak selection on the calibration curve was examined. Moreover, the calibration stability was inspected by splitting the long time measurement in data sets of 25 hours.

The major result of this works is that the deviation of the calibration $\frac{\Delta E}{E}$ amounts to $<0.1\,\%$ over a range of 6 to 60 keV. It is shown that the calibration curve parameters are independent from the fitting range of the individual energy peaks as well as from the number of peaks used for the calibration. Nevertheless, on the 0.1 % level charge sharing events have to be removed from the spectrum as they cause too much asymmetric smearing of the peaks. Also, energy peaks actually consisting of several different peaks were proven to be unsuitable for a precise peak position determination. Furthermore, the long time stability investigation showed that the calibration is time-independent. However, it also demonstrated the need of recording the current of the integrated Field Effect Transistor (FET) of the SDD.

Contents

1 Introduction **5**

1.1 Neutrino Physics 5

1.1.1 Neutrinos in the Standard Model 5

1.1.2 Neutrino Oscillation and Neutrino Mass 6

1.1.3 Sterile Neutrinos 7

1.2 The KATRIN experiment 8

1.3 The TRISTAN project 10

1.3.1 Detector requirements 10

1.3.2 TRISTAN detector design 11

2 TRISTAN detector prototype setup **13**

2.1 Working principle of Silicon Drift Detectors 13

2.2 Experimental setup and prototype detector design 14

2.3 DAQ-settings optimization with Fe-55 18

3 Detector Calibration with Am241 **21**

3.1 Am-241 spectrum analysis 21

3.2 Fitting method 22

3.2.1 Photon response and fit parameter limitations 22

3.2.2 Preparatory energy and resolution calibration 24

3.3 Charge Sharing Cut 29

3.4 Independence of the energy calibration from the fitting range 31

3.5 Investigation of an optimal calibration-peak selection 32

3.6 Estimation of the calibration linearity and error 34

3.7 Long time stability of the energy calibration 36

4 Conclusion and Outlook **39**

Appendix **41**

Introduction

1.1 Neutrino Physics

Neutrinos are neutral elementary particles with three different flavours ν_e, ν_μ and ν_τ, similar to their charged leptonic parnters e, μ and τ. They take an extraordinary place in the Standard Model (SM) of elementary particles since they are only interacting via weak interaction and have no right-handed partner. In this section the neutrino will be introduced by giving a short overview of its discovery as well as its fundamental properties. Furthermore, neutrino oscillation will be described as well as how its observation leads to a non-zero neutrino mass requirement. Subsequently, the possibility of the existence of a right-handed neutrino, the so-called sterile neutrino, and its role as a candidate for dark matter will be discussed.

1.1.1 Neutrinos in the Standard Model

The existence of neutrinos was first postulated by Wolfgang Pauli in 1930 in order to explain the observed continuous spectrum of the β-decay, while two monoenergetic lines were predicted. The neutrino was finally discovered in 1956 by Frederick Reines and Clyde Cowan, as they detected the neutrino flux from a nuclear reactor via inverse β-decay on protons:

$$\overline{\nu}_e + p \rightarrow e^+ + n \tag{1.1}$$

During the next 20 years also the ν_μ and the ν_τ have been observed. Hence, three neutrino flavours exist alike their charged leptonic partners e, μ and τ. [1]

Neutrinos are part of the Standard Model (SM) of elementary particles, presented in figure 1.1. The SM consists furthermore of six quarks of different flavours and three charged leptons, which all exist with left- and right-handed chirality. Nevertheless, the neutrino takes a special place as it is the only particle exclusively interacting via weak interaction. Since this interaction only couples to left-handed particles and neutrinos are electrically neutral, a possible right-handed neutrino would not interact at all with other Standard Model particles. Therefore, only left-handed neutrinos had been detected, which are assumed as massless within the Standard Model.

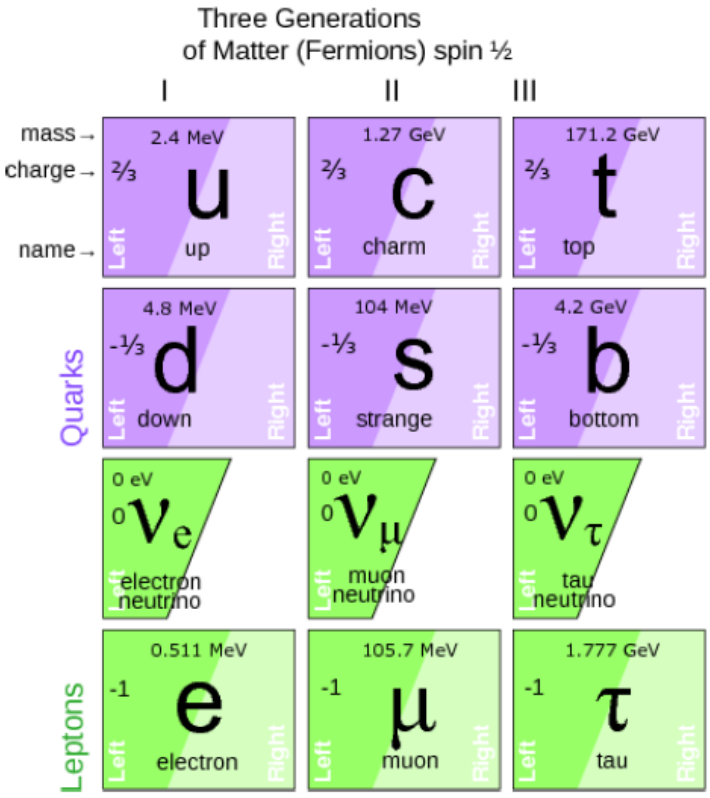

Figure 1.1: **Standard Model of elementary particles.** The six quark flavours are presented in purple and the six leptons, separated in charged and uncharged leptons with three flavours each, in green. Every particle exists with left- and right-handed chirality except the neutrino. It is introduced in the Standard Model as solely left-handed and massless. (Adapted from [2])

1.1.2 Neutrino Oscillation and Neutrino Mass

After it was possible to detect solar neutrinos in the 1960s by experiments like GALLEX [3], the so-called solar neutrino problem occurred. All experiments only saw one third of the expected neutrino rate. The SNO experiment [4] measured all neutrino flavours via neutral current interaction. It observed that the total neutrino rate was consistent with the solar model, while the flavours were not.

To explain this observation, the theory of neutrino flavour mixing was introduced. It describes the phenomenon that the three flavour eigenstates are a superposition of three mass eigenstates, also known as neutrino oscillation. Neutrinos are produced and interact in their flavour eigenstates $(\nu_e, \nu_\mu, \nu_\tau)$ but propagate in their mass eigenstates (ν_1, ν_2, ν_3). The mixing can be described by the Pontecorvo-Maki-Nakagawa-Sakata (PMNS) matrix:

$$\begin{pmatrix} \nu_e \\ \nu_\mu \\ \nu_\tau \end{pmatrix} = \begin{pmatrix} U_{e1} & U_{e2} & U_{e3} \\ U_{\mu 1} & U_{\mu 2} & U_{\mu 3} \\ U_{\tau 1} & U_{\tau 2} & U_{\tau 3} \end{pmatrix} \cdot \begin{pmatrix} \nu_1 \\ \nu_2 \\ \nu_3 \end{pmatrix} \tag{1.2}$$

The probability to oscillate from a produced flavour eigenstate α in the measured eigenstate β for two flavours can be calculated by equation 1.3. Here L is the travelled distance, E the energy of the neutrino, Θ the mixing angle between the mass eigenstates and Δm^2 the difference of the squared masses of the mass eigenstates. This equation can be easily adapted to all three neutrino flavours [5].

$$P_{\alpha\to\beta} = sin^2(2\Theta) \cdot sin^2\left(\frac{\Delta m^2}{4E} \cdot L\right) \tag{1.3}$$

To describe the solar problem, neutrinos need to oscillate. This is only possible in the case where at least one Δm^2 is larger than zero and therefore not all neutrinos can be massless. Unfortunately, neither the absolute mass of the neutrinos, nor the hierarchy of the mass eigenstates can be determined through neutrino oscillation. Observations of reactor, accelerator and atmospheric neutrinos confirmed neutrino oscillation. The current best measurements are $\Delta m^2_{12} = (5.43 \pm 0.18) \times 10^{-5}$ eV^2 and $\Delta m^2_{23} = (2.41 \pm 0.05) \times 10^{-3}$ eV^2.[6]

After experiments analysing neutrino oscillation could determine Δm^2_{12} and Δm^2_{23}, there still remains the question of the absolute neutrino mass. From cosmology observations regarding the overall mass density of the universe and its structure, model dependent upper limits for the neutrino mass can be calculated. These limits though range from $m_\nu < 0.73\,\text{eV}$ to $m_\nu < 0.12\,\text{eV}$ (at 95 % C.L.).[6] The KATRIN experiment, however, aims to directly measure the neutrino mass with a sensitivity of 0.2 eV (at 90 % C.L.) via the β-decay spectrum of tritium.[7]

1.1.3 Sterile Neutrinos

The Standard Model (SM) can be expanded by a new type of neutrino, the sterile neutrino. This could be the right-handed partner of the known purely left-handed neutrinos and is referred to as 'sterile' because it would not take part in any SM interaction. Its existence can introduce a mechanism to give neutrinos mass via the Sea Saw mechanism [8] leading to a heavy sterile neutrino in the mass range of GeV and very light active neutrinos. Sterile neutrinos in an eV-scale can clarify several experimental phenomena like the reactor anomaly.[9] In this work the focus will be set on a keV-scale sterile neutrino as it represents a candidate for dark matter.

From cosmological observations we estimate that the universe consists to 68 % of dark energy, 27 % of dark matter and 5 % of baryonic matter. Dark energy describes a form of energy responsible for the expansion of the universe and dark matter a non-luminous form of matter only weakly interacting. The SM does not provide any suitable candidates that are electrically neutral and stable in respect of the age of the universe. However, sterile neutrinos with masses in the keV-scale could be a good candidate for warm and cold dark matter. Astronomical observations set model dependent constraints to the allowed sterile neutrino mass and mixing angle. The current limits on the parameter space are $1\,\text{keV} < m_s < 50\,\text{keV}$ and $10^{-3} < sin^2(2\theta_s) < 10^{-7}$ in the case the entire dark matter would be made out of sterile neutrinos. [7]

To crosscheck these limits, laboratory based experiments aim to directly search for a keV sterile neutrino. The TRISTAN project, an expansion of the KATRIN experiment, purposes to probe the sterile parameter space up to masses of 18.6 keV with a sensitivity of $sin^2(2\theta_s) < 10^{-6}$ measuring the β-decay spectrum of tritium.[10] Although this region is largely excluded by cosmological observations, a direct and model independent search with laboratory conditions is worth the effort.

1.2 The KATRIN experiment

The KArlsruhe TRItium Neutrino experiment (KATRIN) was developed to measure the neutrino mass through the β-decay spectrum of tritium. Its main setup consists of two parts, the Source and Transport Section (STS) and the Spectrometer and Detector Section (SDS), resulting in a roughly 70 m long KATRIN beamline. In this section the experimental setup is briefly described. An overview can be seen in figure 1.2. Further information can be found in the KATRIN design report [11].

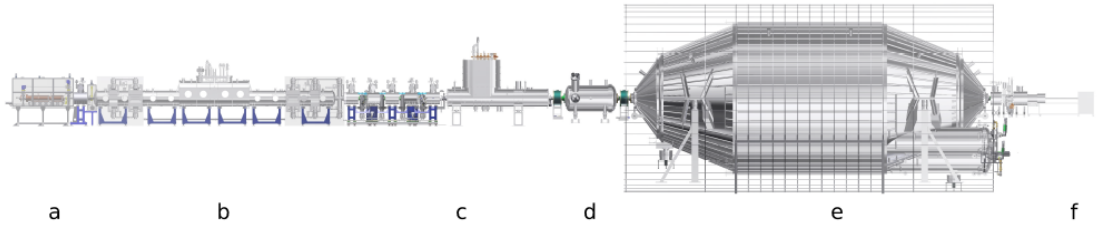

Figure 1.2: **KATRIN experimental setup.** (a) rear section, (b) Windowless Gaseous Tritium Source (WGTS), (c) transport section, (d) pre-spectrometer, (e) main spectrometer, (f) Focal Plane Detector (FDP). (Figure taken from [7].)

Source and Transport Section (STS)

The KATRIN experiment uses molecular tritium gas for several reasons. First of all, tritium has a relatively short half-life of 12.3 years, which provides high signal rates with low source densities. This minimizes the source-related systematic effects, like inelastic scattering, and provides the statistics needed to reach the aimed sensitivity. Furthermore, a precise theoretical description of the spectral shape is possible because the tritium β-decay is of super-allowed type. Last but not least, with its low endpoint energy of 18.575 keV the tritium β-decay spectrum is suitable to search for sterile neutrinos in the lower energy region of astronomical interest. [7]

In the Windowless Gaseous Tritium Source (WGTS) highly stable tritium gas is injected, cooled to 30 K and circulated in a closed inner loop. It is not separated from the remaining system in order to minimize energy loss through scattering. The tritium is held at constant activity level by removing decay products and adding fresh tritium. Like this, the purity is held over 95 % and the decay rate is stable at 10^{11}Bq with maximal variation of 0.1 %.[12] A solenoid transports decay-electrons towards the main-spectrometer. Two pumping stages in the transport section prevent tritium gas and ions, produced in the de-

cay or by scattering, reaching the SDS. This avoids major background effects and energy loss of the electrons because of scattering. [1]

Spectrometer and Detector Section (SDS)

The pre-spectrometer and the main spectrometer are MAC-E filters (Magnetic Adiabatic Collimation and Electrostatic retardation), acting as high-pass filter, only allowing electrons with sufficiently high energy pass towards the detector, by creating a negative electrical potential in the middle of the spectrometer (also known as analysis plane). Two superconducting solenoids at the ends of the spectrometer create an inhomogeneous magnetic guiding field. The energy resolution only depends on the ratio of the magnetic field strength of the analysis plane and the pinch magnet: $\frac{\Delta E}{E} = \frac{B_A}{B_{max}}$. The use of the pre-spectrometer is to reduce the flux of β-electrons entering the main-spectrometer, while the main-spectrometer is filtering by energy. [1] [12]

The Focal Plane Detector (FPD) is a monolithic 148-pixel silicon p-i-n diode wafer. The pixels are equal sized and arranged in twelve concentric circles, consisting of 12 pixels each, surrounding four bull's eye pixels. It is located within the detector magnet at the downstream side of the main spectrometer. The magnet focuses the electron beam on the 90 mm diameter active detection area. As it is designed to reliable detect electrons at low rates, the maximal measurement rate is 62 kcps. [12]

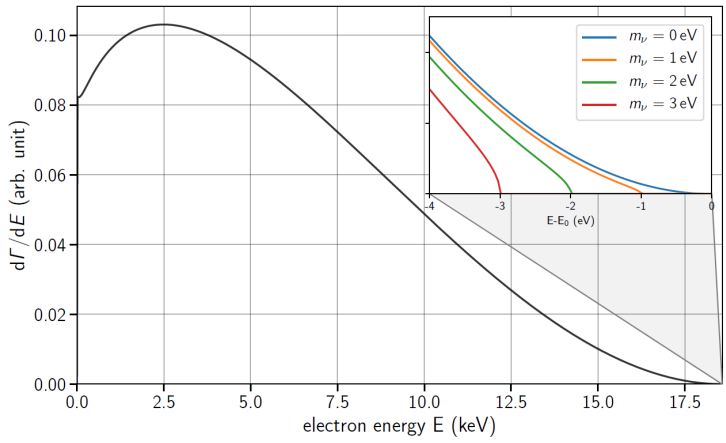

Figure 1.3: **Neutrino mass signature in the tritium β-decay spectrum.** Tritium β-decay spectrum is depicted with the imprint of the effective electron anti-neutrino mass, which shifts the endpoint energy to lower energies. The effect is shown for different neutrino masses. (Plot adapted from [13]).

The total energy E_0 set free in the tritium β-decay divides between the electron and the electron anti-neutrino. Therefore, the maximal energy of the detected electron is $E_e = E_0 - m_\nu$. As a result, the neutrino mass can be seen at the end of the spectrum by a shift from the endpoint energy, illustrated in figure 1.3. The KATRIN experiment aims to measure the effective electron anti-neutrino mass with a sensitivity of 0.2 eV at 90 % C.L. with an integral measurement. It measures the count rate for different retarding potentials of the main spectrometer. By doing so, the experiment already derived an upper limit for the neutrino mass of 1.1 eV (90 % C.L.) [14] which improved previous upper limits by

factor of two after a measuring period of only four weeks. [7]

1.3 The TRISTAN project

The TRitium Invetigations of STerile to Active Neutrino mixing (TRISTAN) project is an expansion to the KATRIN experiment. By upgrading the detector section with a Silicon Drift Detector (SDD) array it aims to search for keV sterile neutrinos. The TRISTAN detector will replace the FPD and aims to probe the sterile parameter space up to masses of 18.6 keV and down to mixing angles of $sin^2(\Theta) < 10^{-6}$ with three yeas of data taking using a differential measurement method.[10]

1.3.1 Detector requirements

A fourth neutrino mass eigenstate results in an additional sterile neutrino flavour. This leads to the superposition of the β-decay spectrum due to the light effective mass term m_{light} of the active neutrinos and the possibly heavy mass eigenstate m_s of the sterile neutrino. For $E_e < E_0 - m_s$ tritium β-decay in a keV-scale sterile neutrino is energetically allowed and results in a kink in the spectrum at $E_{kink} = E_0 - m_s$, conceptually presented in figure 1.4. A small mixing amplitude $sin^2(\Theta)$ of 10^{-7}, whereas Θ is the mixing angle between active and sterile neutrino, still leads to a clearly measurable kink and a pronounced spectral distortion for $E_e < E_{kink}$. [7]

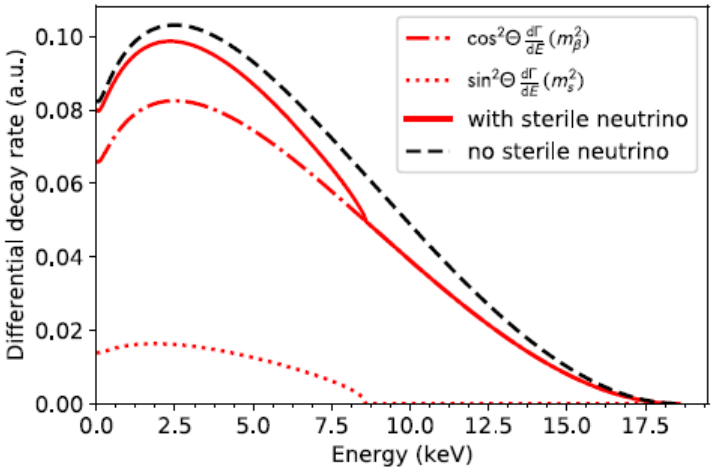

Figure 1.4: **Sterile neutrino signature in the tritium β-decay spectrum.** Theoretical tritium β-decay spectrum with imprint of a sterile neutrino with $m_s = 10$ keV and $sin^2(\Theta) = 0.2$, which is unphysical but emphasises the kink. The red dotted lines portray the sterile and the active part of the spectrum. The black dotted line shows the spectrum without a heavy neutrino mass eigenstate. (Figure taken from [10])

The possible statistical sensitivity with the TRISTAN detector are mixing angles ranging from $sin^2(\Theta) = 10^{-6}$ to $sin^2(\Theta) = 10^{-8}$.[12] Sensitivity studies, thoroughly described in [7], show that the imprint of the kink-like structure is stronger for the differential mode. Therefore, the retardation potential of the main spectrometer is lowered to an area, where

the sterile neutrino mass is estimated. The energy of the electrons is measured by the detector, instead of filtered by the main spectrometer. This leads to some major problems for the KATRIN detector system and the need of an expansion by the TRISTAN detector.

First, instead of one count per second for an energy region of 1 eV above the endpoint energy, approximately 10^8 counts per second will reach the detector within the aimed TRISTAN source strength. This extremely high count rate has to be handled by the detector and therefore be distributed among many separate pixels. [13]

Furthermore, the entire spectrum has to be understood to the parts-per-million (ppm) level. Therefore, it is necessary to precisely comprehend the detector response and have a detector with excellent energy resolution. Calculations have shown that an energy resolution with $\Delta E < 300\,\text{eV}$ Full Width Half Maximum (FWHM) at 30 keV is required in order to reduce the smearing of the kink.[13] In this respect, Silicon Drift Detectors (SDDs), whose working principle is explained in section 2.1, are proven to be very convenient. [12]

Electrons lose their energy continuously travelling through matter. Unfortunately, energy they deposit near the entrance window of SDDs, in the so-called dead layer, cannot be recognized by the detector system. This leads to a shift to lower energies, degrading the energy resolution. Hence, a dead layer of $< 100\,\text{nm}$ is wanted.[12]

Also, a small out-gassing rate is headed for as it reduces the likeliness of a second dead layer through condensed molecules on the detector and limits the reachable pressure. [13]

Additionally to a good energy resolution, an excellent energy calibration is a crucial part in understanding the detector response. Since it is one of the most fundamental properties of the detector, it sets the basis for all further investigations. Furthermore, variations in the overall calibration can lead to additional smearing and shifts of the spectrum. In this thesis the margin of error introduced by the calibration is investigated. Moreover, the calibration stability over nine days was examined.

1.3.2 TRISTAN detector design

Taking all requirements for a sterile neutrino search into account, a design for a detector had been developed. The TRISTAN detector will be a multi-pixel Silicon Drift Detector. SDDs are known for their excellent energy resolution close to the Fano-limit, high rate capabilities and being suitable to be operated in strong magnetic fields. [13]

The detector will be 20 cm in diameter and consist of 21 rectangular modules with 166 SDD pixels each. The pixels will be 3 mm in diameter, arranged in a honeycomb pattern because of their hexagonal shape. Like that, charge-sharing is minimized by making the pixels as large as possible without compromising the energy resolution. [13]

The modules will be mounted on copper blocks with two front-end electronic boards on each side, as pictured in figure 1.5. To reduce electronic noise, the copper blocks are cooled to $-30\,^{\circ}\text{C}$. [13]

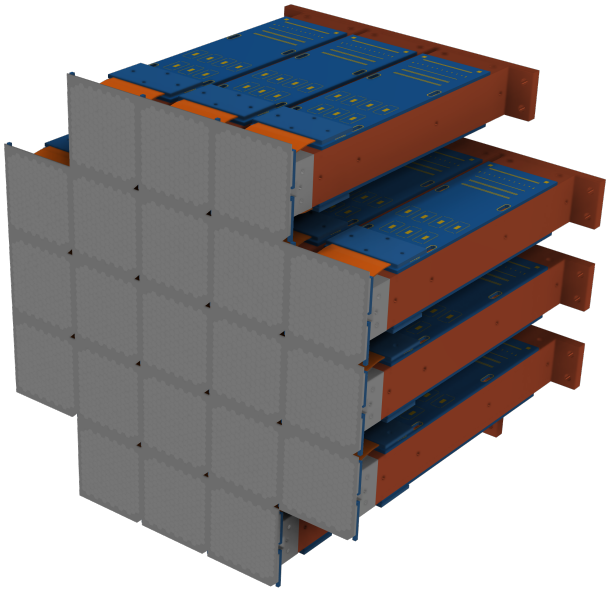

Figure 1.5: **TRISTAN detector design.** 21 modules with each 166 SDD pixels (grey) are mounted on copper blocks (brown) with two front-end electronic boards on the sides (blue).

TRISTAN detector prototype setup

In order to develop the TRISTAN detector, a small seven-pixel prototype detector was produced to characterize the detector's properties and optimize the electronic readout chain. The working principle of a Silicon Drift Detector (SDD) as well as the experimental setup for the prototype detector are the topics of this chapter. Additionally, the optimization of the Data AcQuisition System (DAQ) concerning noise reduction and false event triggering will be discussed in this chapter.

2.1 Working principle of Silicon Drift Detectors

Silicon Drift Detectors are able to detect X-rays as well as electrons at high counting rates with an excellent energy resolution. They consist of a semiconductor PIN (positive, intrinsic, negative) diode, composed of differently doped electrodes on each side of the detector. On the entrance window side is p^+-type silicon. It is usually doped with phosphorus, which serves as an electron donator, since it has five valence electrons in contrast to silicon, which has four. On the bottom side a small n^+-doped anode is placed in the centre. It is usually doped with boron, which has only three valence electrons and therefore functions as an electron acceptor. This structure leads to a so-called depleted area, which is the region near the junction. Here, each phosphorus atom has donated an electron, which was each accepted by a boron atom. Inside the depletion zone there are no free charged particles present any more. With a high enough voltage U_{bias} applied to the SDD this depleted area can be extended over the entire detector. [1] [12]

The energy E_{pair} required for the creation of an electron-hole pair in silicon is 3.67 eV.[15] An ionizing particle with $E > E_{pair}$ can interact with valence-band electrons in silicon and excites them into the conduction band, creating an electron-hole pair. Hence, the depleted area forms the active detection area. The produced charge carriers are proportional to the energy of the incoming particle. They are guided by an electric field towards the anode, which is created by p^+-doped drift rings surrounding the anode. Therefore, the anode can be very small which results in a low capacitance and reduces the noise respectively. A sketch of the SDD structure can be seen in figure 2.1. [1] [12]

In the SDDs used for TRISTAN a Field Effect Transistor (FET) is integrated. It works as pre-amplifier sensitive to the charge collected at the anode and converting it to a voltage output. The capacitance is minimized through this anode-FET combination due to avoiding conventional bond pads, again ensuring minimal noise. [16]

An important characteristic of SDDs is their excellent energy resolution, which is close to

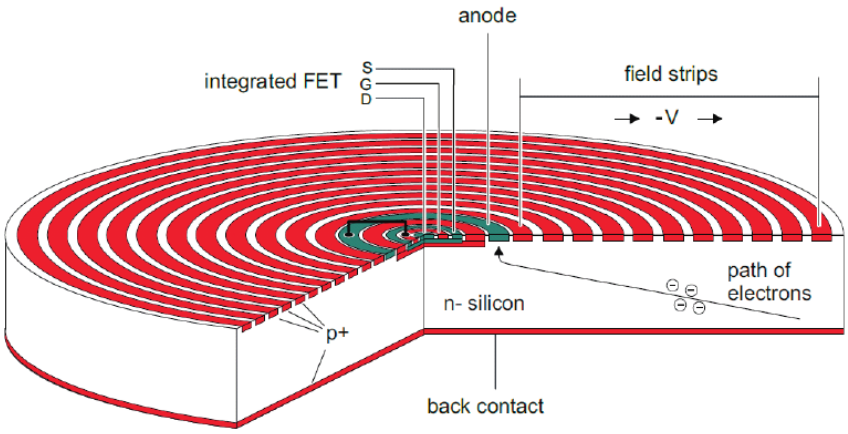

Figure 2.1: **SDD working scheme.** The small n^+-doped anode and the integrated FET are colored in green. Shown in red are the back contact (p^+-doped) and the drift rings (n^+-doped). The exemplary path of the electrons generated by an incoming particle, is visualized as well. (Taken from [13])

the Fano limit for the TRISTAN prototype detectors. It describes the statistical fluctuations in the charge generating process and can never be surpassed. The variance of the peak for incoming particles of a certain energy is therefore the sum of the Fano-variance and the variance of the electronic noise (σ_{el}) arising from the detectors' readout chain. This can be calculated as follows:

$$\sigma_{Fano+Noise} = \sqrt{F \cdot w \cdot E_0 + \sigma_{el}^2} \tag{2.1}$$

Here F is the Fano factor, which is slightly temperature and energy dependent, and is set to 0.117 [15] within this work. The energy necessary for creating an electron-hole pair in silicon is referred to as w. It is assumed as 3.67 eV for an experimental setup cooled to 245 K.[15] As one can see in formula 2.1, for decreasing energies the resolution of the peaks improves.

One inevitable effect that additionally decreases the energy resolution in SDDs is the dead layer. In this area close to the detector surface not all electric field lines end up at the detector anode. This means that only part of the energy or none at all is registered at the anode. It results in a lower signal as well as lower energy detected than expected. Hence, a dead layer as thin as possible is desirable. [12]

2.2 Experimental setup and prototype detector design

The prototype detector, fabricated by the Semiconductor Laboratory (HLL) of the Max Planck Society, is placed on the detector board and consists of seven hexagonal 3 mm large pixels. The pixels' shape ensures that there is no space between the pixels, which eliminates dead detection areas. To provide the best energy resolution, the signal of the SDD should be amplified as soon as possible. Therefore, a FET is integrated in the SDD

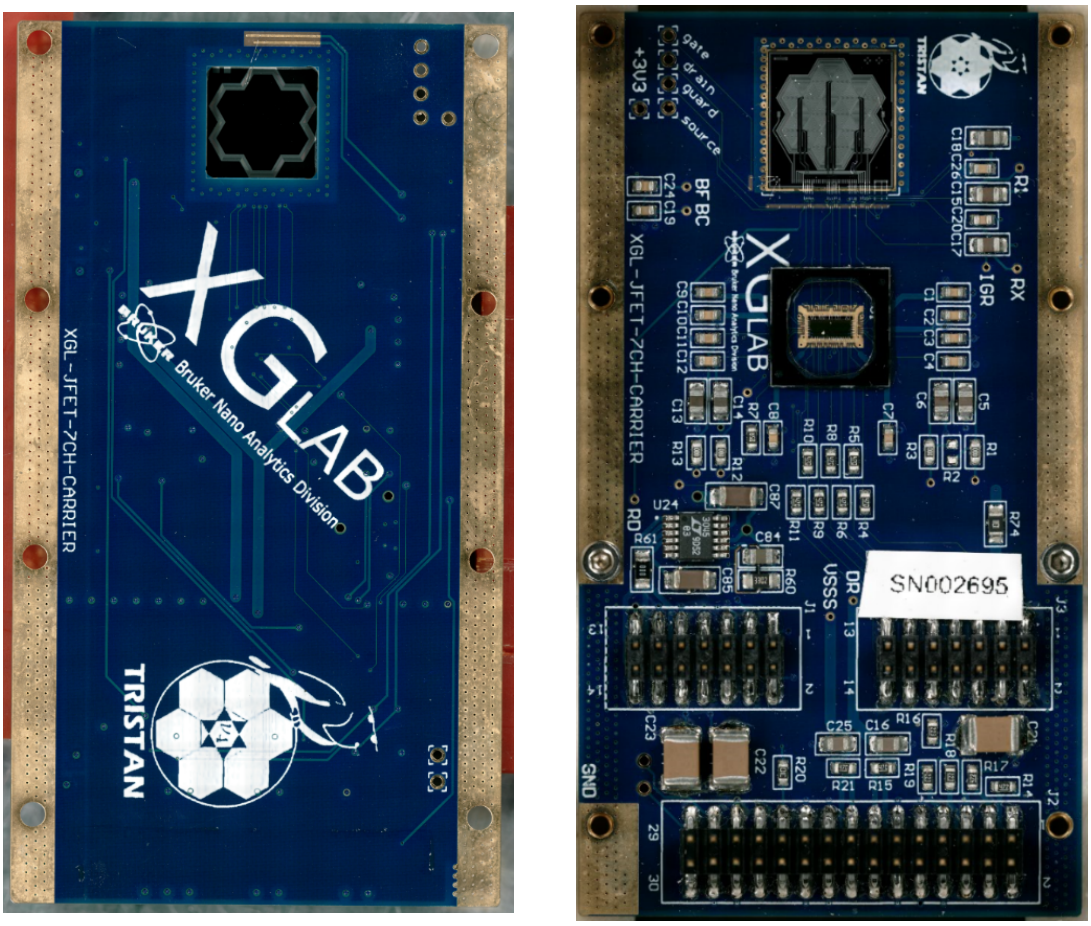

Figure 2.2: **Detector board with the seven pixel prototype detector.** On the left: The entrance window side of the detector board is shown. The seven hexagonal pixels can be seen in the middle of the top. On the right: The top side of the detector board is pictured, where the pixels and the ETTORE pre-amplifier directly beneath are visible.

and an ETTORE pre-amplifier is also placed on the detector board. The detector board can be seen in figure 2.2, whereas the pixels numeration is illustrated in figure 2.3.

The detector board is mounted onto a copper holding structure, which allows for different distances and angles of the detector to the examined source. It is thermally coupled to a cooling plate, which is connected to an external chiller. The cooling is necessary to reduce the leakage current of the detector, improving the energy resolution. In order to avoid condensing of molecules from the surrounding air onto the detectors' surface due to the cooling, the whole holding structure is placed into a vacuum chamber. Otherwise it could destroy the SDDs or result into an additional dead layer. The vacuum reaches pressures down to 10^{-7}mbar, preventing electrons from the source to get absorbed by the air. [12] [17] [18] The interior of the vacuum chamber is pictured in figure 2.4.

The detector board is connected to the bias board, which in turn is attached to the power supply. The bias board, produced by XGLab, provides all voltages for the SDD, as well as power supply for the ETTORE. Since the waveform is continuously increasing because of the leakage current of the detector, the bias board is responsible for a synchronous

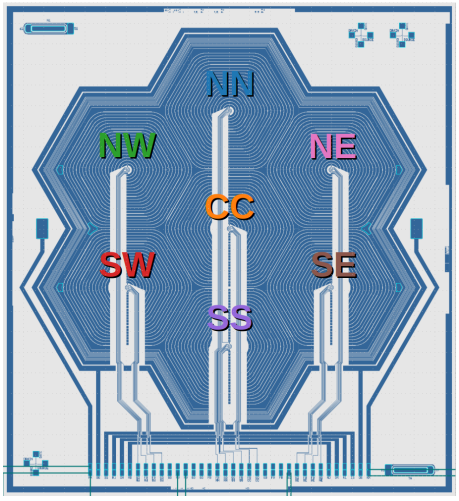

Figure 2.3: **Pixel map.** The pixels are enumerated by compass directions **N**orth, **E**ast, **S**outh and **W**est. The **C**entral pixel is defined as CC.

reset signal for all pixels, when the waveform of one pixel reaches a preset threshold. The bias board also serves as additional amplifier, before the signal is passed on to the Data AcQuisition System (DAQ). [12]

A exemplary waveform is shown in figure 2.5, where the reset can be seen as a steep decline of the signal on both sides of a ramp created by the leakage current in the SDD. An event appears as sharp step on this ramp, as an interacting particle creates many electrons in a short period of time. The height of the step corresponds to the energy of the detected incoming particle.

The bias board is connected to the DANTE DPP (Digital Pulse Processor), also fabricated by XGLab. It digitizes the waveform with an 16-bit Analog-to-Digital Converter (ADC) with a sampling rate of 125 MHz. To evaluate the energy of an event, the DPP analyses the waveform with two trapezoidal filters. A fast filter marks possible events above a preset threshold. A second more accurate trapezoidal filter precisely determines the energy of the found event. More information about the working method of trapezoidal filters can be found in [19]. The events can be saved, inter alia, in a histogram or a list with the time stamp and the energy of each event. [12]

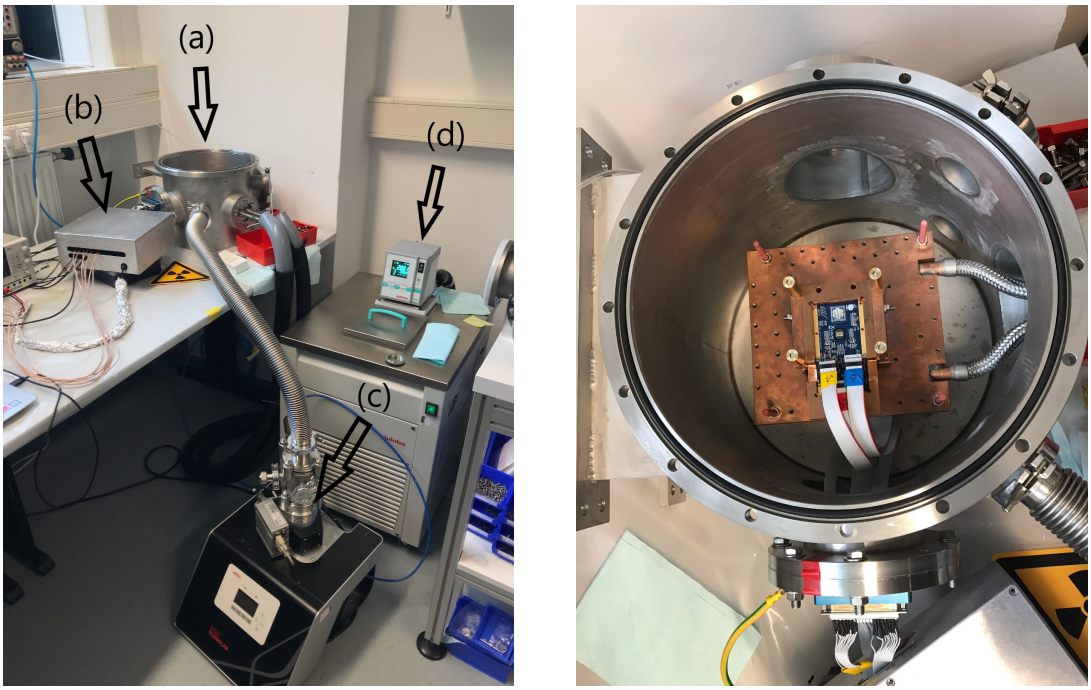

Figure 2.4: **Experimental Setup.** On the left side: (a) Vacuum chamber, (b) bias board, (c) vacuum pump, (d) cooling system; On the right side: The detector board (blue) is mounted on the copper holding structure, which is connected to the cooling system. The setup is mounted in a vacuum chamber and the detector board is connected with cables to the bias board outside the vacuum chamber.

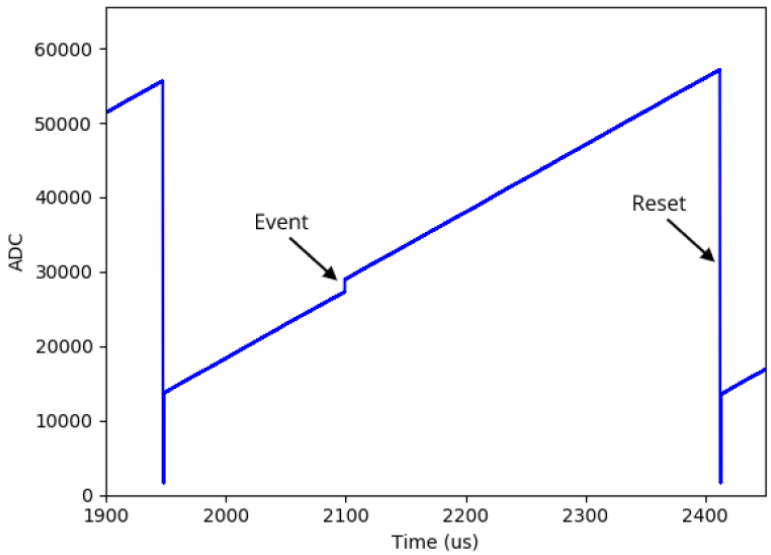

Figure 2.5: **Exemplary waveform.** The leakage current of the SDD results in a continuous increase of the waveform. On this ramp an event appears as sharp step. To prevent saturation of ETTORE, a reset signal is sent to all pixels by the bias board, when one of the waveforms reaches a preset threshold. (Taken from [12])

2.3 DAQ-settings optimization with Fe-55

To record data, the influence of noise always should be as small as possible. Therefore, the DAQ settings have to be optimized in terms of the energy peaking time of the trapezoidal filter and the threshold estimated to identify events. The different noise components of the detector system as well as their dependence on the systems' constituents and the temperature is further examined in [19].

In order to do these optimizations, an Fe-55 source was used. It has a sufficiently short half-life of 2.73 years and decays through electron capture to Mn-55. The exited Mn-55 looses its surplus energy especially by emitting X-rays of 5.9 keV (Mn-K_α) or 6.5 keV (Mn-K_β) or Auger electrons of 5.9 keV. In the used source the Auger electrons cannot penetrate the sources' shielding and are therefore not detected. [18]

First of all, the peaking time of the trapezoidal filter was optimized. The peaking time should be as low as possible to enable the DAQ to handle high count rates. For too low peaking times the noise from the pre-amplifiers lowers the energy resolution, while for too high peaking times the current noise takes over.[17] The data was taken in sweep mode, where only one parameter is varied, in this case the peaking time. Here, the Fe-55 spectrum was measured for 300 s for each peaking time. Then the Full Width Half Maximum (FWHM) of the Mn-K_α peak is determined, while its relative position to the Mn-K_β peak is used for energy calibration. By plotting the FWHM as a function of the peaking-time, as shown in figure 2.6, an optimal energy resolution of approximately 220 eV at 2.3 µs peaking time at 25 °C can be obtained.

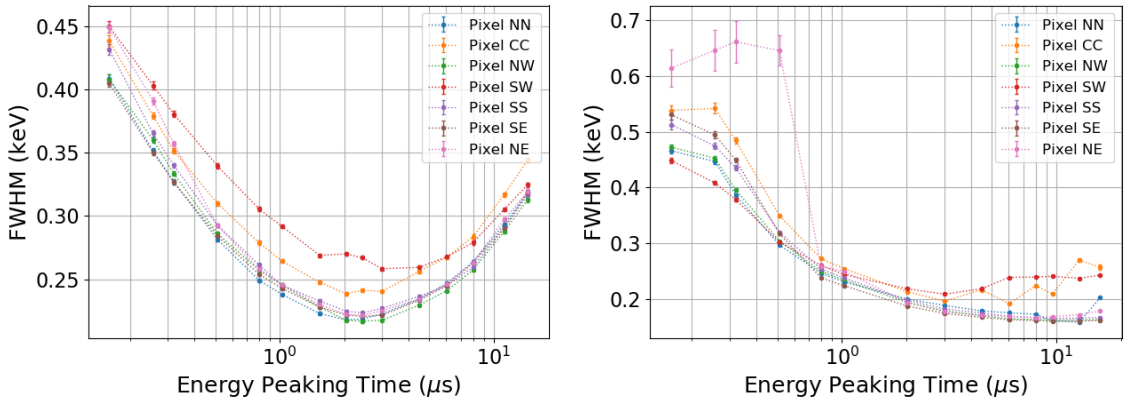

Figure 2.6: **Energy peaking time sweep for different temperatures.** On the left: The FWHM is plotted as function of the energy peaking time for all seven pixels at 25 °C. The optimal peaking time for the best energy resolution of 220 eV is at about 2.3 µs at the minimum of the curve. On the right: The same measurement is processed at −30 °C which reduces the leakage current and therefore improves the energy resolution at high peaking times.

For the system cooled to -30°C the leakage current decreases, which also can be seen in figure 2.6 on the right side. Hence, at 2.3 µs peaking time the FWHM is approximately 180 eV. As the main measurement for this work was taken with a cooled system, with a

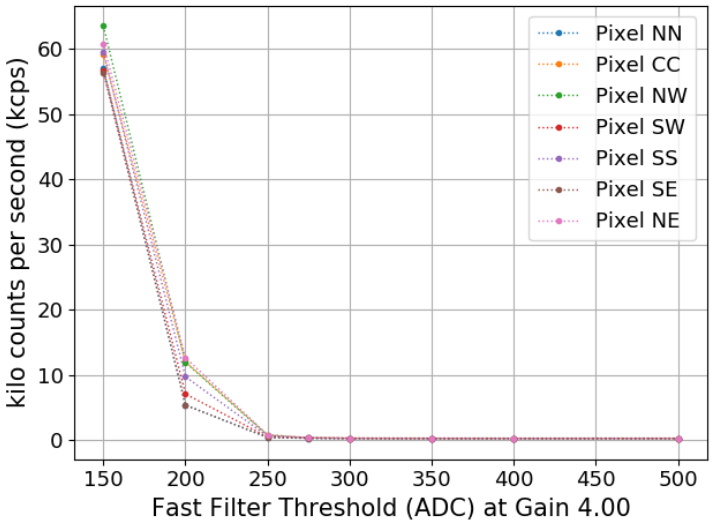

Figure 2.7: **Fast filter threshold sweep at** 25 °C**.** For higher thresholds the count rate of the detected events decreases, as fewer events get registered by the DAQ. At small thresholds the DAQ triggers on noise.

source of small rate, a higher peaking time of 4 µs with slightly better FWHM of about 160 eV at 5.9 keV was chosen. This value also takes into account that the SW as well as the CC pixel have a worse energy resolution for higher peaking times as the other ones, especially as of approximately 4 µs. Since this work focuses on the central pixel, this had to be considered, although the reasons for this unexpected behaviour are still unknown.

The fast filter threshold is the minimal voltage rise during the peaking time needed for an event to be registered by the DAQ. If the threshold is set too low, the DAQ falsely triggers on noise, increasing the overall deadtime of the system. On the other hand, for higher thresholds more and more real events get discarted. Therefore, the threshold was varied, while all the other parameters were fixed. For each threshold the rate of detected events was measured for 30 s, visualized in figure 2.7. At high thresholds the rate of the source can be evaluated, which in the case of the used Fe-55 source amounts to (0.26 ± 0.02) kcps. The optimal threshold for a low noise trigger rate is about 300 ADC for a gain of 4. For a gain of 1, which was used for the main measurement, this equals to a threshold of 75 ADC (~0.28 keV). Nevertheless, the main long time measurement was taken with a threshold of 180 ADC (~0.67 keV). Since an $^{241}_{95}$Am source does not emit photons in a energy range below 10 keV, this bigger threshold was set to eliminate even more noise.

Detector Calibration with Am241

An excellent energy calibration is essential to understand the detector response as it sets the basis for all further investigations. To hold the margin of error of the calibration as small as possible, a calibration source providing several photon or electron peaks is crucial. Hence, within this work, $^{241}_{95}$Am was used as mono-energetic photon source with almost thirty energy peaks in a range of 0 to 60 keV. This chapter deals with the resulting spectrum after almost ten days of data taking and the analysis of its components. After a fitting method is developed in section 3.2 and a charge sharing cut is applied on the spectrum in section 3.3, an investigation of the calibration is done in respect of the fitting range in section 3.4, the optimal peak selection in section 3.5 and the total error on the calibration in section 3.6. Furthermore, the stability of the calibration over time is examined in section 3.7.

3.1 Am-241 spectrum analysis

$^{241}_{95}$Am is a radioactive side product in nuclear reactors. It decays to $^{237}_{93}$Np via α-decay with a half-life of 432.2 years.[20] The α-particle and simultaneously emitted electrons are stopped in the protective layer surrounding the americium source, in this case consisting of platinum. They therefore cannot reach the detector. To lose its surplus energy, the $^{237}_{93}$Np atom emits photons with energies in the range of keV and above.[20]

These photons also may excite other elements, which emit photons of element-specific energies themselves. This results in so-called fluorescence lines in the spectrum. The main element detected is platinum, as it is used for protecting the source and, hence, is located directly in the travelling direction of the photons to the detector. There are also copper fluorescence lines, because it is used for the holding structure of the detector board. In addition, there are iron fluorescence lines. Iron is the main part of stainless steel, which is used for the mounting of the source, the vacuum chamber as well as the screws. Furthermore, titan and barium peaks can be determined. Their origin is still unknown.

A nomenclature for all peaks, which can be seen in figure 4.1, has been established. It also considers data taken in January 2019 with another detector generation (2 mm pixel detector without integrated FET). The energies of interest within this work are ranging from 0 to 60 keV. The relevant photon energies as well as their relative intensities are summed up in table 4.1 in the appendix.

In figure 3.1 the resulting spectrum of the central pixel after almost ten days of data

taking can be seen. It is an overlap of all photon peaks as well as background effects. The precise photon response is further described in section 3.2. Also, a bump at the end of the spectrum between approximately 48 keV and 55 keV is visible. This phenomenon results from compton scattering of the photons of 59.541 keV in the surroundings of the detector. This way the photons lose up to 11 keV of energy before they reach the detector. Therefore, these photons do not contribute to the peak they originate from but instead lead to the bump at lower energies. Furthermore, the spectrum shows a steep decline at about 0.67 keV ($\hat{=}$ 180 ADC). It ends there due to the set threshold since events that fall under this value are not evaluated. At about 0 keV the noise peak is located. It consists of noise that surpasses the fast filter but is identified as noise by the energy filter.

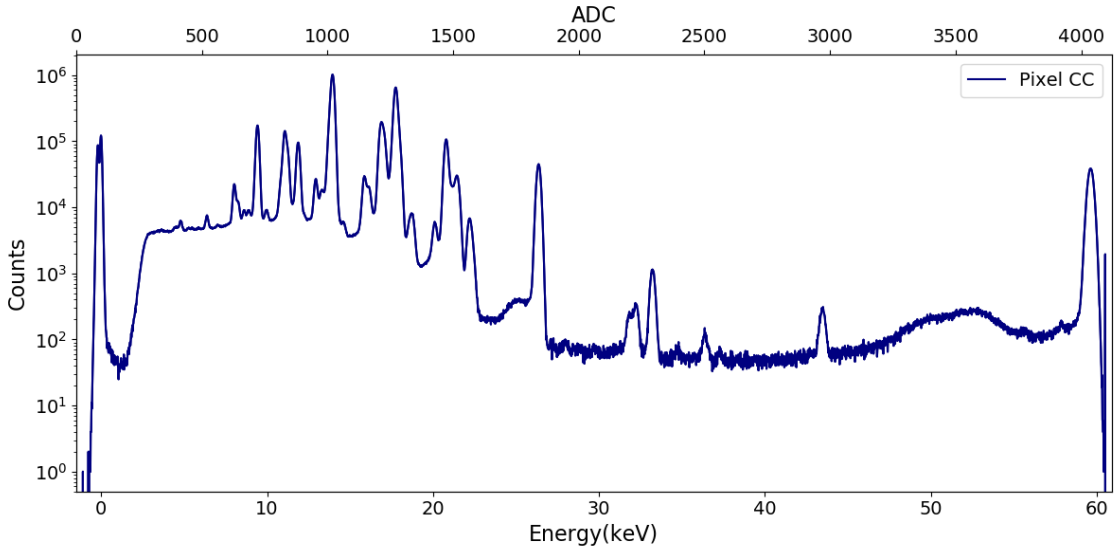

Figure 3.1: **Am-241 spectrum of the central pixel.** The spectrum shows a noise peak on the left hand side at 0 keV, followed by a steep decline due to the threshold settings. All photons from the americium decay as well as fluorescence lines from other elements can be seen together with background effects.

3.2 Fitting method

The recorded spectrum has numerous peaks. To ensure that every peak position is evaluated correctly, one has to have a closer look at the response function of mono-energetic photons. This warrants an accurate energy calibration of the detector system. Furthermore, a fitting principle has to be developed. Moreover, fit parameter constraints have to be set to guarantee the reproducibility of the results as well as the quality of the fits.

3.2.1 Photon response and fit parameter limitations

The detection of a mono-energetic photon results in a Gaussian peak in the spectrum. The width of the Gaussian function, indicated in equation 3.1, is only dependent on electronic noise and the Fano limit as introduced in section 2.1. Here E_0 stands for the energy of the

incoming photon and A for the amplitude of the Gaussian peak. The higher the photons' energy the more likely it is that it penetrates the silicon bulk of the detector without interacting. Therefore, the detected signal intensity, corresponding to the amplitude of the Gaussian function, is reduced in comparison to the emission probability of the photon.

$$G(E) = A \cdot exp\left(-\frac{(E - E_0)^2}{2\sigma^2}\right) \tag{3.1}$$

Photons interact point-like with matter via absorption, in contrast to electrons which continuously interact with matter while travelling through it. Therefore, their energy is very likely either be fully detected or not at all when they leave all their energy in the dead layer. Nevertheless, there are small border effects when the charge cloud extends into the insensitive area. As the entrance window is much smaller than the detectors' thickness, these effects are negligible for the determination of the peak position. However, they contribute to the spectrum, as well as the scattering of the created electrons while they drift to the anode. These effects appear as a shoulder on the low energy side of the peaks forming the major background.

Charge sharing events contribute to the background as well. They lead to a smearing of the lower energy side of the peak resulting in an asymmetry. Since, these events can be removed from the spectrum their effect can be mostly eliminated. The origin from charge sharing events as well as their impact on the peak position is further described in section 3.3.

For every peak, there also exists a second Gaussian peak shifted about 1.74 keV towards lower energies. This is the so-called silicon escape peak, which arises when a Si-K_α photon leaves the SDD without being detected. After all, this effect is much smaller for photons than for electrons and is therefore not visible within the background. The reason for this is that electrons interact closer to the surface in comparison to photons of the same energy. Hence, it is more likely for a Si-K_α photon to leave the detector if it is generated by an electron than a photon.

As a result, every photon peak in the course of this work was fitted with a Gaussian function and a constant background (cf. figure 3.2). Some of the peaks are a superposition of two or more peaks. If two peak positions are less than 30 eV apart, the peaks are not fitted by one Gaussian function each. The reason for this is that fitting programs are incapable of finding both peak positions properly, when they are this close together. Instead, they are treated within this work as one Gaussian peak. Its peak position is then the average of the two actual peak positions weighted by their relative intensities.

In order to prevent the fit from diverging, some limitations are set on the fit parameters. The background is estimated on the left hand side of the regarded peak on an approximately flat spectrum space. In the following fitting process it is allowed to vary about 5 %. The peak position is initialized by the expected photon energies which is converted in ADC through a rough pre-calibration further described in section 3.2.2. It is allowed to vary about 380 eV (25 ADC) in both directions. Furthermore, the amplitude is fixed to be positive. The sigma of the Gaussian function is prescribed to lie within 0 and 760 eV (50 ADC). The value for sigma transferred to the fit as initial guess is specified in advance

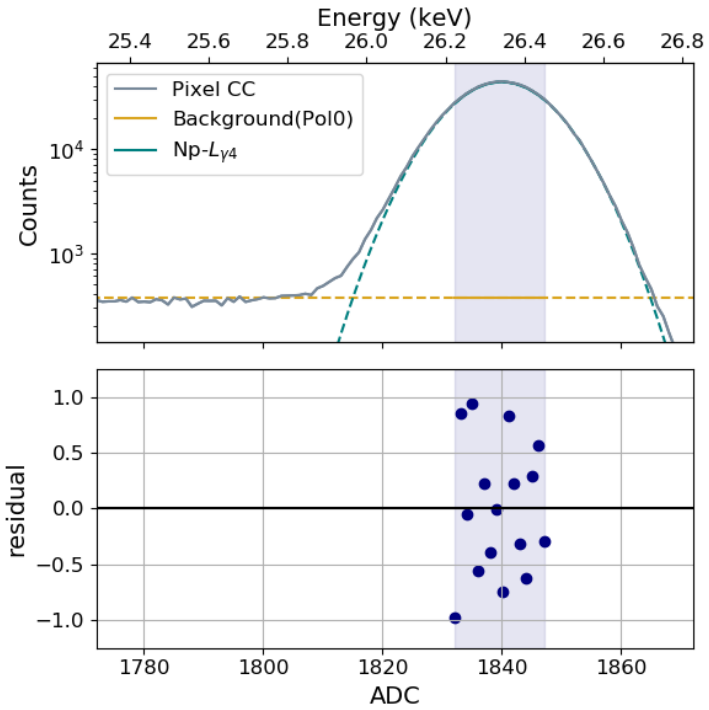

Figure 3.2: **Exemplary Gaussian fit.** Peak 28 (cf. 4.1) is fitted with a constant background (yellow) and a Gaussian function (green). The fitting range is highlighted in blue. The residuals of the fit are given in units of standard deviations in the figure below.

by a sigma assessment as described in section 3.2.2.

If two peaks are close together but too different to be assumed as one peak, a reduced Gaussian model is applied. This means that two correlated peaks are fitted. Their relative amplitude is fixed relying on the peaks' relative intensities. The peak position of the first peak is allowed to vary 150 eV (10 ADC), while the second position is passed as the absolute distance to the first peak. This distance is given by the energy difference, once again converted in ADC by the pre-calibration. It is allowed to vary about 50 %. The sigma parameter for both peaks is assumed as equal and limited as described above.

In a few cases more strict constraints were necessary, especially if one peak consists of several peaks. However, any set limitation just helps the fit to converge without having impact on the peak position.

3.2.2 Preparatory energy and resolution calibration

The conversion from ADC to energy E is done by a linear function with two open parameters, a slope s and the offset o on the y-axis (cf. equation 3.2).

$$ADC = s \cdot E + o \tag{3.2}$$

For a calibration of the spectrum with all available peaks, it is useful to do a pre-calibration. For this single peaks with high visibility best spread over the whole spectrum are suitable.

Keeping this in mind a selection of six peaks is taken, which are listed in table 3.1. Actually, the iron peak consists of two peaks, but since they only differ by 13 eV, their peak position is averaged and fitted as one. There is not any other better suitable single peak in this low energy region. Taking this pre-calibration step simplifies finding all other peak positions with a minimal effort. The location of the peaks as well as their fits can be seen in figure 3.3.

Element	Name	Energy (keV)
${}_{26}$Fe	K_α	6.400
${}^{237}_{93}$Np	L_l	11.871
${}^{237}_{93}$Np	Gamma (1)	26.345
${}^{237}_{93}$Np	Gamma (3)	33.196
${}^{237}_{93}$Np	Gamma (4)	43.423
${}^{237}_{93}$Np	Gamma (5)	59.541

Table 3.1: Selected pre-calibration peaks with their energies

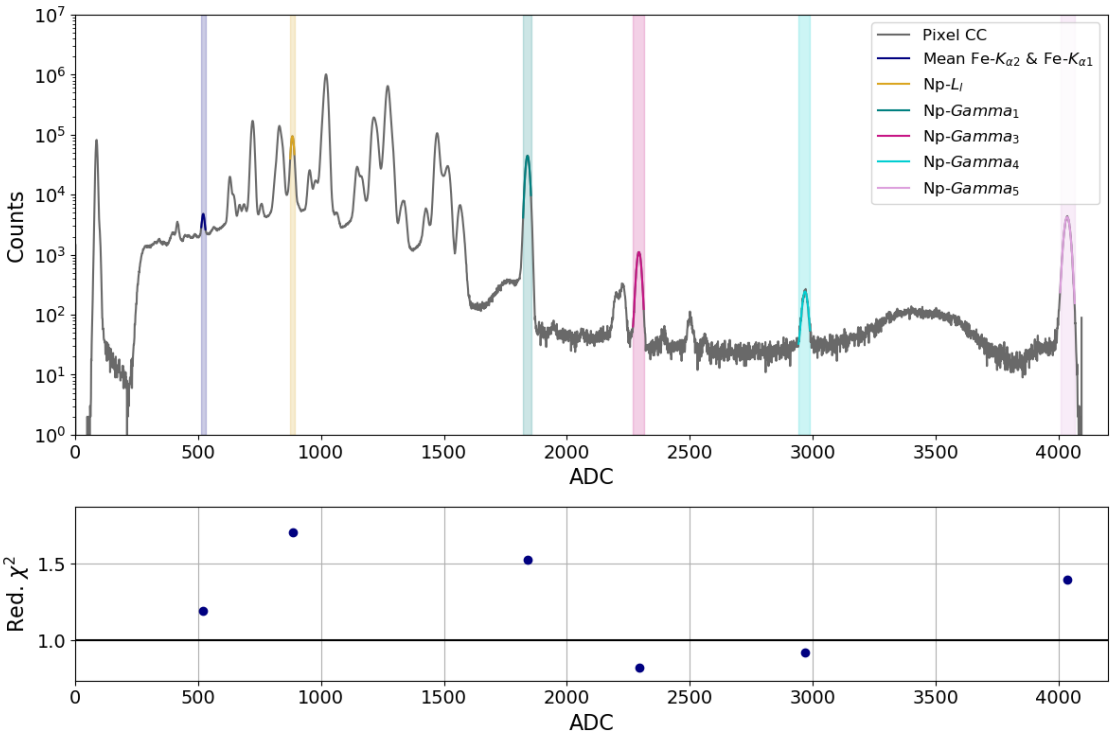

Figure 3.3: **Peak selection for a rough pre-calibration.** The selection of six single peaks used for a pre-calibration as well as their fitting range are visualized by different colours. To get an overview of the quality of the fits, the reduced χ^2 for each fit is presented in the graph below.

In figure 3.4 the resulting calibration curve is presented. For this the six pre-calibration peaks were fitted and each peak position in ADC was matched the relevant photon energy. Subsequently, a fit was applied according to equation 3.2. For this purpose, a charge

variable	value
s	$(66.12 \pm 0.01)\,\frac{\mathrm{ADC}}{\mathrm{keV}}$
o	$(98.14 \pm 0.31)\,\mathrm{ADC}$
σ^2_{slope}	$0.000\,17\,\frac{\mathrm{ADC}^2}{\mathrm{keV2}}$
$\sigma_{slope,offset}$	$-0.003\,55\,\frac{\mathrm{ADC}^2}{\mathrm{keV}}$
σ^2_{offset}	$0.093\,98\,\mathrm{ADC}^2$

Table 3.2: Fit results of the pre-calibration

sharing cut was applied. The method to identify charge sharing events as well as their impact on the determination of the peak position are further described in section 3.3.

The estimation of the error of this calibration is as well depicted in figure 3.4. The calibration error is minimal at about 10 keV and continuously increases for higher energies. It can be calculated by using the co-variance matrix of the fit pursuant to equation 3.3. The diagonal entries of the matrix are named σ^2_{slope} and σ^2_{offset} and the off-diagonal entries, which describe the correlation between slope and offset, are referred to as $\sigma_{slope,offset}$. All fit results from the calibration are given in table 3.2.

$$\sigma_E(ADC) = \sqrt{\sigma^2_{slope} \cdot x^2 + \sigma_{slope,offset} \cdot x + \sigma^2_{offset}} \tag{3.3}$$

The pre-calibration peaks were each fitted with a sufficiently large fitting range in order to determine the energy resolution. This has several advantages. First of all, the deviation of the energy resolution in respect to the Fano limit can be identified. Therefore, the electronic noise can be determined by a fit to the energy resolution at different energies according to equation 2.1 (cf. figure 3.5). The resulting σ_{el} accounts for $(59.84 \pm 1.53)\,\mathrm{eV}$. Furthermore, the energy resolution can also be used to pass the Gaussian fit an initial guess for σ. This increases the probability that the fit converges.

In order to make the individual fits comparable, the fitting range for every peak will be specified in units of these pre-estimated σ within this work. If several peaks are fitted together the fitting range is determined as the peak position of the first peak minus σ to the peak position of the last peak plus σ. Therefore, also the behaviour of slope and offset for different fitting ranges can be evaluated. This is investigated in section 3.4.

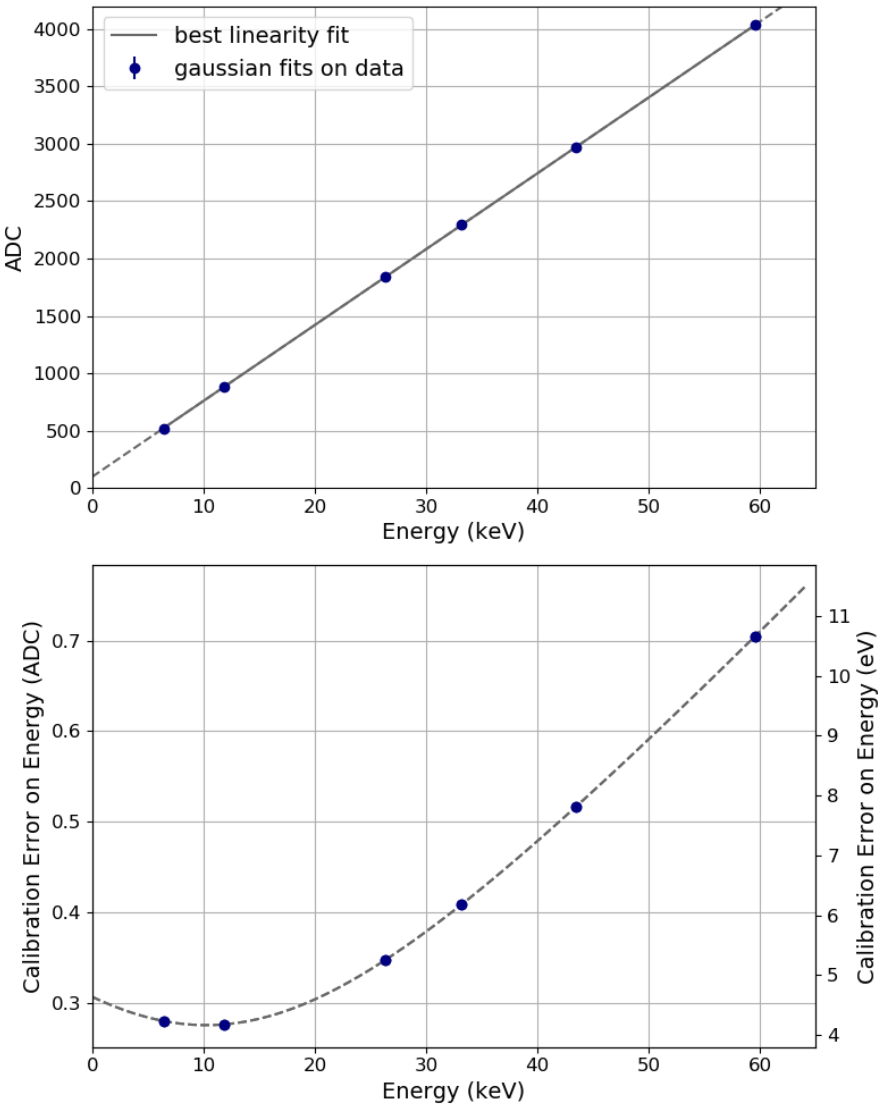

Figure 3.4: **Pre-calibration curve with estimation of the absolute calibration error.** On the top: The pre-calibration curve of $^{241}_{95}$Am with six considered peaks is shown as well as the underlying data points. The slope amounts to $(66.12 \pm 0.01)\,\frac{\mathrm{ADC}}{\mathrm{keV}}$ and the y-offset to (98.13 ± 0.31) ADC. On the bottom: The calibration error has been estimated. The error is smallest for low energies and continuously increases for high energies. The minimal calibration error is at about 10 keV.

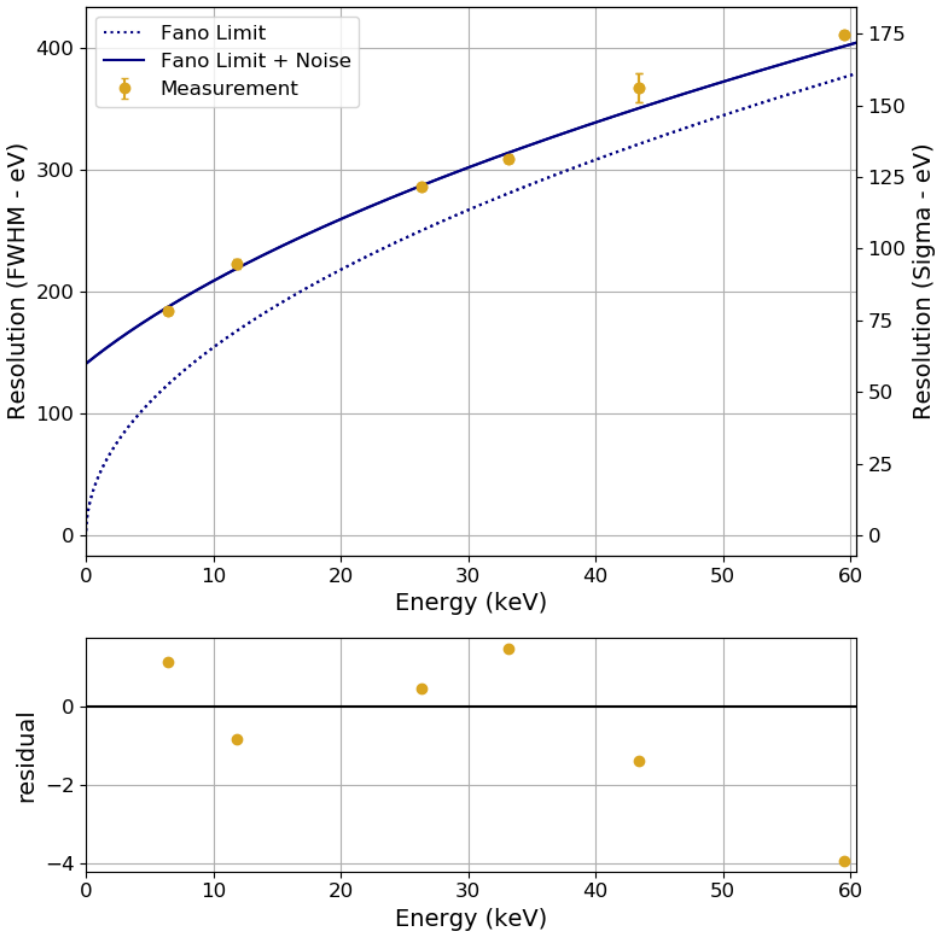

Figure 3.5: **Fano-plot based on the pre-calibration peaks.** The energy resolution for every pre-calibration peak is plotted in yellow. The blue line is the fit on this data, while the dotted blue line shows the Fano limit. On the right hand side the resolution is translated in units of sigma. As expected, the energy resolution is worse for higher energies. From the fit an electronic noise of $\sigma_{el} = (59.84 \pm 1.53)\,\mathrm{eV}$ can be evaluated. At the bottom the residuals are given in units of standard deviations.

3.3 Charge Sharing Cut

To calibrate the detector, it is necessary to precisely model the peak position of each identified energy coming from the source. To simplify the detector response model required for each peak, a charge sharing cut is applied. It reduces the complexity of the measured spectrum and simplifies the fitting procedure. Especially, since charge shared events have an asymmetric effect onto the peak shape towards lower energies, removing this variable makes the fitting procedure much more stable and reliable.

A charge sharing event is an event which happens very close to the border of two pixels. The charge cloud created by the incoming particle gets divided and directed to two different anodes because of the electric field of the drift rings. Hence, an event is detected at approximately the same time in both pixels. The detected energy in each pixel, however, is smaller than the incoming particle originally had. To classify these charge sharing events, a time window can be defined. It determines that two events happening within this time range in two different pixels are correlated to one charge sharing event.

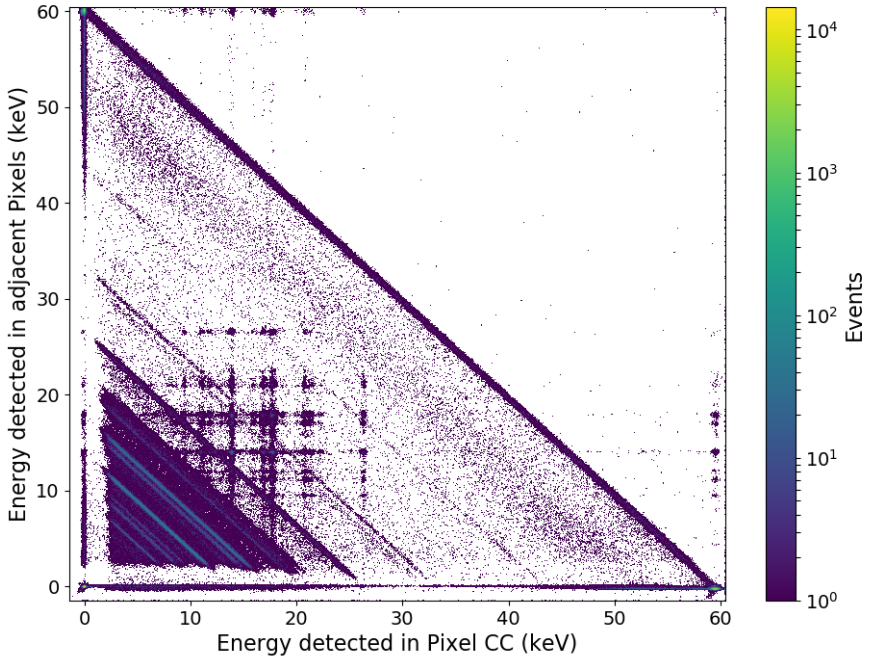

Figure 3.6: **Identified charge sharing events between the central pixel with every adjacent pixel for a time window of 125 ns.** For a time window of 125 ns all identified charge sharing events of the central pixel with adjacent pixels are plotted in a 2D histogram. The diagonal line depicts the correctly identified charge sharing events while the check pattern can be determined as random coincidence. On the left and bottom side wrongly identified events can be seen. The impact of the threshold shows itself as roughly blank lines alongside.

In the 2D histogram in figure 3.6 all events which happened in the central pixel, with the condition that a second event appeared within a time window of 125 ns in any other adjacent pixel, are illustrated. As charge sharing means that the energy of the incoming

particle is divided arbitrary among two pixels, many of such events result in a diagonal line in the 2D histogram. The check pattern which can be seen in figure 3.6 arises from random coincidences. This means that two particles by chance arrived approximately at the same time at the detector and are falsely tagged as charge sharing events.

At the bottom and the left side of the 2D histogram one can see events wrongly identified as charge sharing, as the whole particle energy is measured in one pixel but a second trigger onto the noise happened in another pixel. Cutting this events of the spectrum will not only lower the energy peaks' height but also reduce the noise peak. The almost blank spaces next to this wrongly defined charge sharing events are a result of the threshold. They correspond to the threshold cutoff next to the noise peak in figure 3.1.

Charge sharing worsens the energy resolution as the lower energy side of the peaks is continuously smeared. Therefore, it also contributes to the background of all peaks on the lower energy side of the regarded peak. As a result, cutting charge sharing events out of the spectrum improves the energy resolution and reduces asymmetric effects of the peak shape. This makes the peaks more distinguishable and lowers the background especially at low energies, making peaks better visible or even discoverable at all.

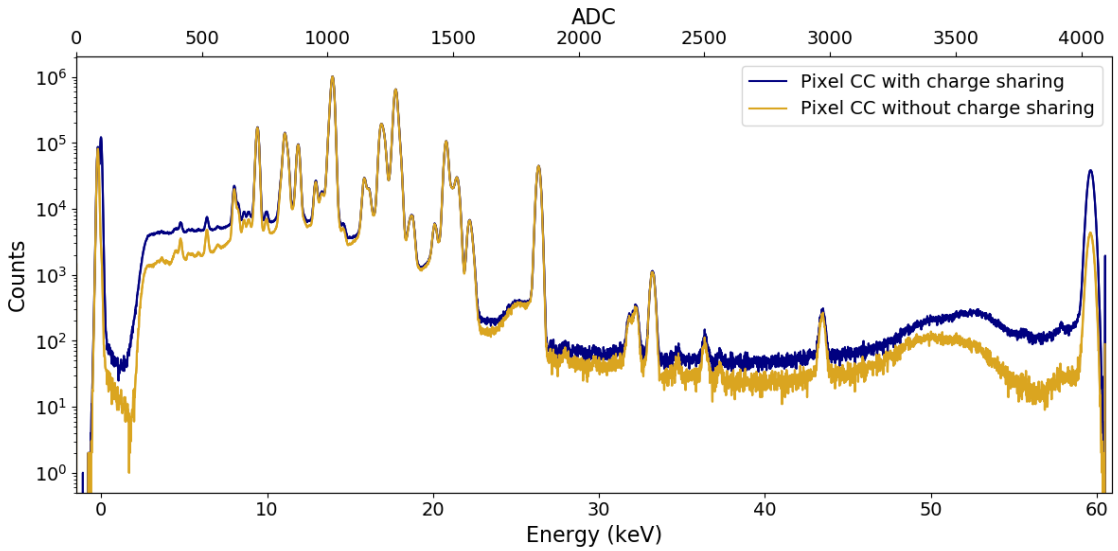

Figure 3.7: **Comparison of the spectrum with and without charge sharing events.** Applying a charge sharing cut on the spectrum reduces the background on the lower energy side as well as improves the energy resolution. Therefore, peaks get more distinguishable or even discoverable at all.

In figure 3.7 the difference between the recorded spectrum and the resulting spectrum with a charge sharing cut applied to it can be seen. A time window of 125 ns was chosen, as it identifies most of the charge sharing events without wrongly identifying to many complete events as charge sharing events. An investigation of the correlation between the time window and the proportion of correctly identified charge sharing events can be found in [21]. A second condition demands that the total energy detected in both pixels refers to a predicted photon energy. It may prevent the cut of random coincidences out of the spectrum. Nevertheless, almost ten days of data taking provides enough statistics so that

the loss of random coincidences due to the charge sharing cut does not affect the spectrum negatively. Therefore, the second condition is not applied within this work.

Performing an energy calibration for both spectra shows the impact of these events on the position of the peaks. For this a selection of five single peaks is chosen. The motivation for this selection is further discussed in section 3.5. The fits are performed in a fitting range of $\pm 1\,\sigma$. In table 3.3 the results for slope and offset of the calibration curves are summarized. There is a slight difference between both results, which is larger than the margin of their errors.

	slope	offset
with charge sharing	$(66.1838 \pm 0.0005)\,\frac{\text{ADC}}{\text{keV}}$	(96.80 ± 0.02) ADC
without charge sharing	$(66.1561 \pm 0.0021)\,\frac{\text{ADC}}{\text{keV}}$	(97.08 ± 0.06) ADC

Table 3.3: Comparison of the energy calibration curve parameters with a selection of five peaks for data with and without charge sharing events

The calibration curve gets more flat and the offset slightly increases when the charge sharing events are taken off the data. Charge sharing leads to an asymmetric main peak which needs to be taken into account for a precise reconstruction of the peak position for the desired accuracy. Due to the many overlapping peaks and the complex background model which is also effected by charge sharing, precisely modeling these asymmetric effect was not possible in the timeframe of this thesis. Therefore, the Gaussian model was assumed, where the peak positions probably are shifted to lower energies by the fitting algorithm to compensate this asymmetry. This results in a steeper calibration curve for data with charge sharing events than without.

Hence, charge sharing events have an impact on the calibration and should be removed from the data. Nevertheless, cutting this events off the data results in bigger uncertainties for the calibration parameters as it means a loss of statistics.

3.4 Independence of the energy calibration from the fitting range

As described in section 3.2 the Gaussian fits are now performed in fitting ranges in units of σ. For this all available stable peaks are used. This means that especially peaks actually consisting of several peaks are not considered. That applies also to multiple peak areas which have to be fitted together, as they are as close together that they influence each other in a significant extent. In detail this exclusion affects peak number 12, 13, 14, 15, 16, 20, 21, 24, 25, 30 and 31 [4.1].

To generate figure 3.8 the energy calibration with the remaining peaks is executed for different fitting ranges. Hence, the corresponding slope and offset of the calibration curve are portrayed. It can be seen that the fitting range has no bigger impact on the calibration because the slope as well as the offset are lying within their errors on a straight line. Fitting this constant line results in $s = (66.155 \pm 0.001)\,\frac{\text{ADC}}{\text{keV}}$ and $o = (97.05 \pm 0.03)$ ADC.

As the calibration curve is now proven to be independent of the fitting range, a sigma of 1

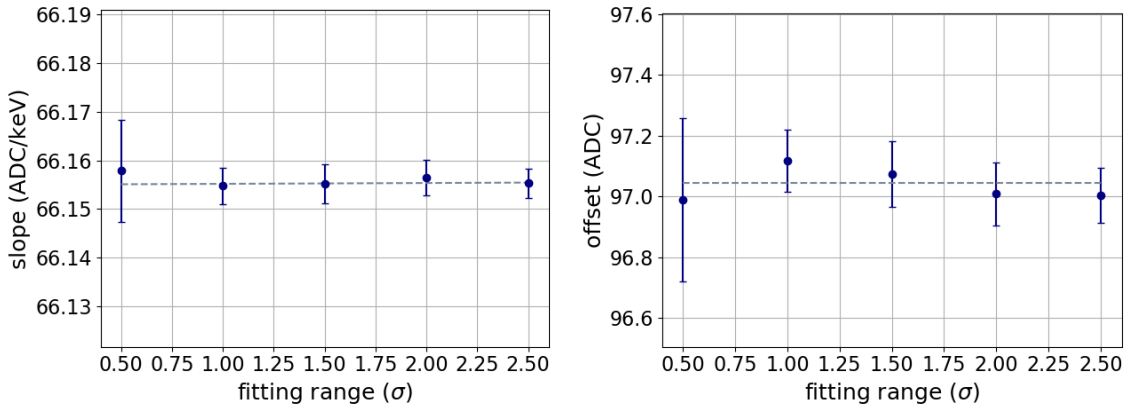

Figure 3.8: **Energy calibration results for different fitting ranges.** Slope and y-offset of the energy calibration curve for different fitting ranges are on a straight line within their errors. The calibration can therefore be assumed as independent of the fitting range. A balance line evaluates $s = (66.155 \pm 0.001)\,\frac{\text{ADC}}{\text{keV}}$ and $o = (97.05 \pm 0.03)\,\text{ADC}$.

is chosen for further peak position evaluations. This range is also based on the fact that for a fit with a simple Gaussian function, not considering further effects like the foothills of the background shoulder, a small range is preferred. A small fitting range, though, provides less data points for a fit leading to bigger uncertainties (cf. figure 3.8). That makes the fit unsuitable to precisely determine the peak position. Within the peak selection for the fitting range investigation bigger ranges have no positive influence. However, for the excluded peaks bigger fitting ranges lead to instabilities of the fits what makes them unusable. Hence, the question arises which peaks are suitable for a good energy calibration. This question is answered in section 3.5.

3.5 Investigation of an optimal calibration-peak selection

Not all peaks in the spectrum are equally suitable for an energy calibration. Peaks that are very close together influence each others peak positions. Therefore, the response model is more complex and the uncertainty of the peak position is larger. Hence, a selection of peaks based on the insight of the photon response and its background is made. In addition, by analysing the calibration results for a different number of calibration peaks one can also express a statement if it is necessary to consider all existing peaks.

For selection one all big single peaks which are clearly separated from any other peak were chosen. In contrast, selection two consists of either small single peaks or single peaks close to other peaks. Category three and four differentiate between visually distinguishable or non-distinguishable double peaks, whereby the latter were fitted by a reduced Gaussian model as described in section 3.2. Barium and titan are treated specially in selection five, as their origin is still unexplained. Moreover, they are situated in an area with major background. For peaks that consist of multiple peaks, selection six considers the peaks with the biggest intensity. In category seven all remaining peaks are compiled. A visualisation of all selections can be seen in the figures 4.2 to 4.8.

After specifying the peaks order of consideration, several energy calibrations were done whereby each time one selection additionally was taken into account. The results are depicted in figure 3.9.

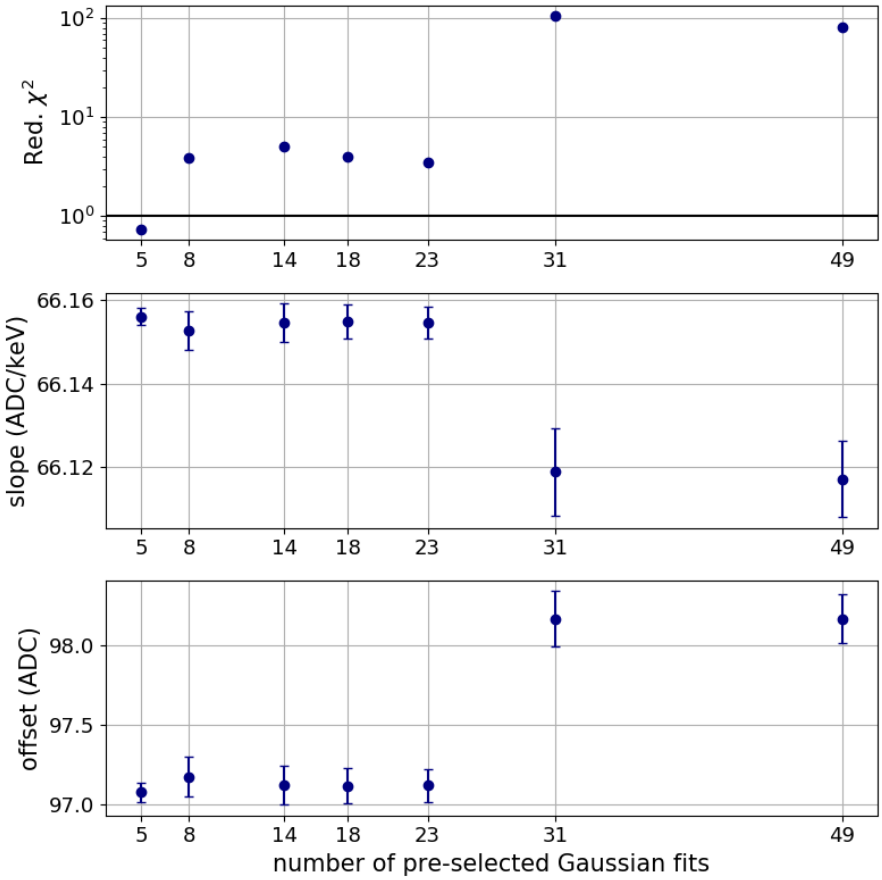

Figure 3.9: **Energy calibration results for different amounts of pre-selected peaks.** The graph shows the reduced χ^2, the slope and the y-offset of the energy calibrations for different numbers of considered Gaussian peaks. The peaks were pre-selected, ranging from big single peaks to peaks consisting of multiple Gaussian peaks. The results remain mainly the same until category six is included. Category six worsens the quality of the calibration fit significantly and visibly shifts the slope as well as the offset.

The reduced χ^2 for an energy calibration with the five peaks of selection one is slightly under a optimal value of one. Taking more peaks into account for the calibration, the reduced χ^2 increases to a value of approximately four and stays mainly the same until selection six is considered. Since a value slightly under or over one is equally fine in terms of the reduced χ^2, the quality of the fit stays the same until selection six is included.

For all peaks including category five the slope and the y-offset remain nearly the same within their error bars. Therefore, the calibration curve for five selected peaks is comparable to one with 23 pre-selected peaks. Since the results of selection one has the smallest error, it is chosen to be the reference calibration for further investigations.

Taking category six and seven into account for a calibration, visibly shifts the slope and

the offset to different values, which results in a more flat calibration curve. Also, the calibration fit is not good since the reduced χ^2 rises to around 100. Hence, both selections are unsuitable for an energy calibration. The peaks consist of too many Gaussian functions to precisely identify the position of each one separately. Their fits are, in addition, not stable for different fitting ranges and need more strict limitations than the others to actually converge at all.

As a result, a selection of five single peaks is sufficient for a precise energy calibration, whereas the peaks chosen for selection six and seven are unusable in this context.

3.6 Estimation of the calibration linearity and error

To evaluate the linearity of the detection system, an energy calibration with the five peaks of category one was made. In figure 3.10 the resulting calibration curve can be seen as well as the position of all peaks of selection two to four onto it. All peaks of selection six and seven are not considered anymore, since they were already excluded to be suitable calibration peaks. Category five was also omitted in the plot, as their peak positions have big uncertainties and bad residuals. Further reasons why they readily can be neglected, had already been given in section 3.5.

The absolute distance of the calibration curve to the data point (residual in units of eV) amounts to $< 30\,\mathrm{eV}$, whereby nearly 90 % of the data points are located within an area of $\pm 10\,\mathrm{eV}$ around zero. One can determine that some peaks have better residuals than others and some also have bigger uncertainties. These peaks can be identified. First of all, peak number 10 (category four) at approximately 9.4 keV has big uncertainties concerning its peak positions. The reason may be that the two peaks it consists of are too close together to properly determine their positions. Peak number 19 at 16.1 keV, which had been assigned to category three, exhibits a peak position not matching the calibration curve as good as the other ones. It is likely that the influence by peak number 20 on its position was underestimated and hence not considered by the fitting model. Moreover, peak number 22 (category four) at approximately 18.7 keV shows big uncertainties. This is possibly an effect of the high energy foothills of peak number 21.

The residuals can also be indicated in percent by dividing the absolute distance of the data points from the calibration curve through the energy of the underlying photon. As a result, the deviation of the calibration of the detector system amounts to $\frac{\Delta E}{E} \approx 0.05\,\%$ at the lowest energy peak at 6.4 keV. It maximally accounts for $\frac{\Delta E}{E} \approx 0.3\,\%$ comparing the calibration curve with the position of all peaks including selection four. Considering that for peak 10 as well as peak 19 the fitting model may not be good enough, it can be argued that the detector system shows a linearity of $<0.1\,\%$ over a range of 6 to 60 keV. This is an excellent result, which also matches the outcome of the investigation of the previous detector generation (cf. [10]).

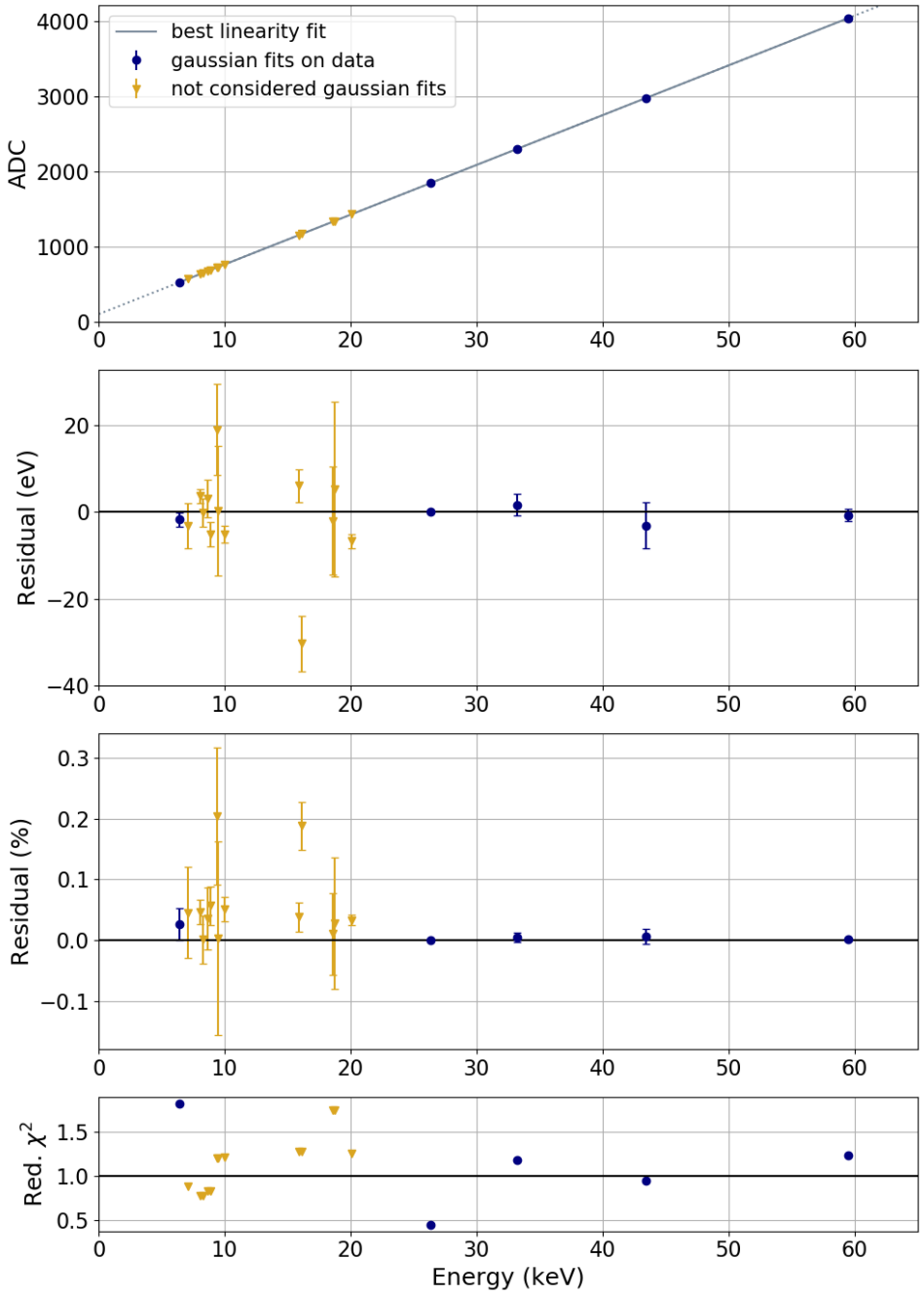

Figure 3.10: **Energy calibration and error estimation with selection one.** The energy calibration was made with selection one (blue dots) and compared to the peak positions from selection two to four (yellow triangles). On the top graph one can see the calibration curve (gray line). The graph below shows the residuals in units of eV, whereby the optimal value of 0 eV is highlighted. For the estimation of the linearity of the detector system, the residuals are given in percent of the respective energy. Within the maximal error bar the linearity amounts to $\frac{\Delta E}{E} \approx 0.3\,\%$. To get an overview of the quality of the individual Gaussian fits of the peaks, the reduced χ^2 are depicted in the bottom graph.

3.7 Long time stability of the energy calibration

Another research subject is the long time stability of the calibration. Therefore, the long time measurement was split into data sets of 25 hours (referred to as 'one day'), which still provide enough statistics to make comparable energy calibrations. Since section 3.3 showed that charge sharing events have an impact on the calibration curve, they are removed from each set of data as described in section 3.3. For every data set a pre-calibration of the energy and the resolution is done. Subsequently, an energy calibration with peak selection one is applied as outlined in section 3.2.

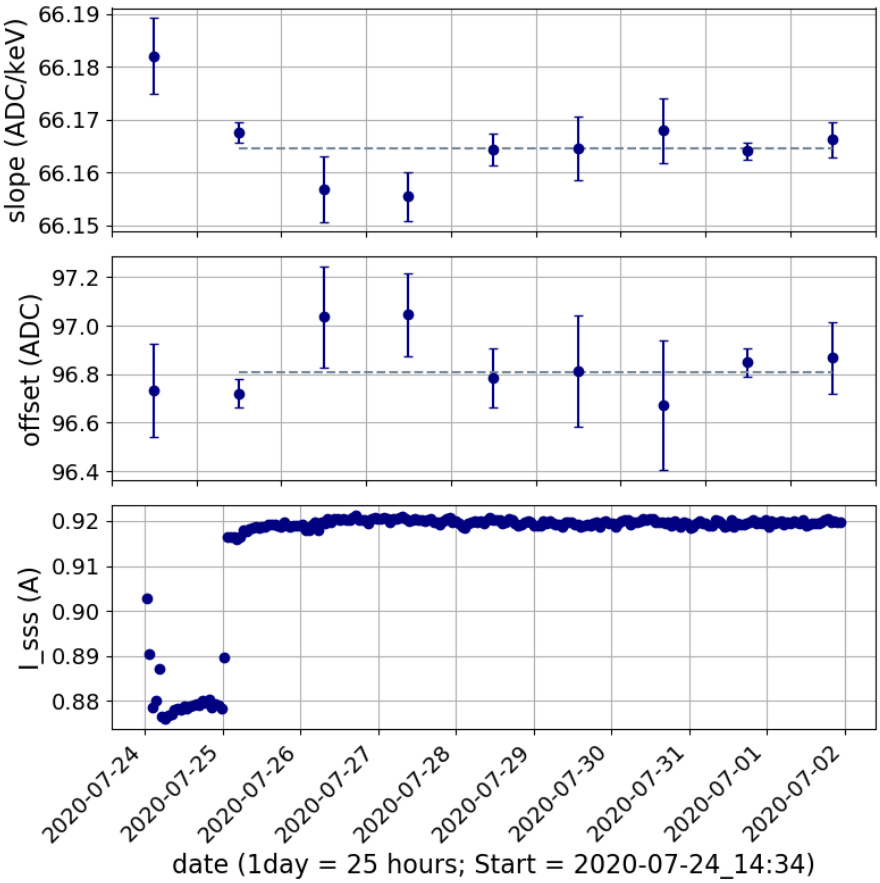

Figure 3.11: **Long time stability investigation.** On the upper two graphs slope and offset for a calibration for data sets each consisting of 25 hours of data are shown. A balance line is indicated in gray, which results in $s = (66.165 \pm 0.001)\,\frac{\text{ADC}}{\text{keV}}$ and $o = (96.81 \pm 0.03)\,\text{ADC}$. The current powering the FET (I_{sss}) is depicted on the lower graph for the whole measuring time.

One can now compare the slope and the offset of the calibration curves of every day as shown in figure 3.11. As expected, both parameters have bigger uncertainties than for a calibration with the whole data as there is less statistics. Slope and offset of the calibration curve for day two to nine are approximately on the same level. However, day one shows a big deviation in the slope in comparison to the other days. This can be explained by the current powering the integrated FET of the SDDs (I_{sss}). In figure 3.11 it is visible

that for day one the current is smaller than for the other days resulting in a weaker pre-amplification of the detector signal. Consequently, the spectrum is compressed to lower ADC leading to a steeper calibration curve with approximately consistent offset. From day one to day two the FET current increases and stays constant afterwards. The reason for this behaviour is still unclear and can also be observed in the current coming back from the FET (I_d). Hence, it is absolutely necessary to record the FET current in parallel to the spectrum.

Nevertheless, neglecting day one, the calibration curve parameters stay approximately constant over time. A balance line fitted on these parameters determines a slope of $s = (66.165 \pm 0.001)\,\frac{\mathrm{ADC}}{\mathrm{keV}}$ and offset of $o = (96.81 \pm 0.03)\,\mathrm{ADC}$. These values are not fitting the parameters for the whole data within their errors. Nevertheless, within the observed energy region it leads to a maximum deviation of both calibrations of approximately 4 eV, which is compatible to the estimated error on the calibration curve shown in figure 3.4. For the peak with the lowest energy this equals to about 0.09 %. Therefore, both calibrations match within the accuracy of the total calibration.

Conclusion and Outlook

In this thesis, the accuracy of the energy calibration was examined. As a first step, all features of a long-time measurement with an $^{241}_{95}$Am source were investigated. Based on this data set, a fitting method has been developed in order to precisely determine the energy peak position. The objects of interest within this work were the dependence of the calibration curve parameters of the fitting range of the peaks, the selection of calibration peaks as well as the impact of charge sharing events. Moreover, the stability of the calibration curve over nine days was examined.

A comparison of the calibration curve for the spectrum with and without charge sharing events at this level of accuracy showed the necessity of a charge sharing cut. Charge sharing events impact the calibration as it leads to asymmetric energy peaks which positions get shifted to lower energies by a simple Gaussian fit. Hence, to avoid this effect on the calibration without a loss of statistics, a more complex fitting model has to be developed.

It was proven that the fitting range has no significant influence on the calibration because the slope as well as the offset are lying within their errors on as straight line for fitting ranges from ± 0.5 to ± 2.5 σ. However, for low fitting ranges the spectrum provides less data points for the fit which is therefore prone to larger errors. Secondly, too large fitting ranges lead to the necessity of a more complex fitting model than a Gaussian function combined with a constant background.

A selection of the peaks by their complexity was performed. On the one hand, calibrating the system with different numbers of pre-selected peaks demonstrated that the calibration curve parameters are mostly independent of the number of calibration peaks. On the other hand, it showed that areas consisting of multiple peaks are too complex to precisely determine the position of each peak separably. They distort the calibration curve and hence should not be used for calibration without improving the model significantly.

It is also worth considering whether one might intentionally add barium in the system. With fluorescence lines in the low-energy range of 4 to 6 keV and in the higher energy range of 32 to 37 keV, it would complement the spectrum well in areas where the americium source does not provide many peaks. Barium was already suspected in the spectrum, but due to its low intensity it was not suitable for calibration purposes.

Using the suitable selection of peaks for the calibration, a maximal deviation from the calibration of $\frac{\Delta E}{E} < 0.1\,\%$ over a range of 6 to 60 keV had been determined. This matches the outcome of the investigation of the previous detector generation. The deviations from the linearity may stem from ADC non-linearities and can possibly be reduced when taking them into account.

Moreover, the calibration curve parameters stay constant over time as shown in figure 3.11. Nevertheless, an anomaly on the first day of data taking pointed out that it is absolutely necessary to record the FET current in parallel to the events.

This thesis lays the groundwork for the future calibration procedure of the TRISTAN detector. Moreover, the validation of the high-linearity and stability of the calibration confirmed the required detector performance, which allows to proceed with the integration of the detectors in the KATRIN beamline.

Appendix

Number	Element	Line	Energy (keV)	Relative intensity	Source
1a	$_{22}$Ti	$K_{\alpha 2}$	4.505	6.4	[22]
1b	$_{22}$Ti	$K_{\alpha 1}$	4.511	12.8	[22]
2	$_{56}$Ba	$L_{\beta 1}$	4.828	2.47	[22]
3a	$_{26}$Fe	$K_{\alpha 2}$	6.391	10.2	[22]
3b	$_{26}$Fe	$K_{\alpha 1}$	6.404	20.2	[22]
4	$_{26}$Fe	$K_{\beta 1,3}$	7.058	3.63	[22]
5a	$_{28}$Ni	$K_{\alpha 2}$	7.461	12.2	[22]
5b	$_{28}$Ni	$K_{\alpha 1}$	7.478	24.0	[22]
6a	$_{29}$Cu	$K_{\alpha 2}$	8.028	13.3	[22]
6b	$_{29}$Cu	$K_{\alpha 1}$	8.048	26.0	[22]
7a	$_{28}$Ni	$K_{\beta 1,3}$	8.265	4.36	[22]
7b	$_{78}$Pt	L_{l}	8.266	0.58	[22]
8a	$_{30}$Zn	$K_{\alpha 2}$	8.616	14.3	[22]
8b	$_{30}$Zn	$K_{\alpha 1}$	8.639	28.0	[22]
9	$_{29}$Cu	$K_{\beta 1,3}$	8.905	4.69	[22]
10a	$_{78}$Pt	$L_{\alpha 2}$	9.362	1.26	[22]
10b	$_{78}$Pt	$L_{\alpha 1}$	9.443	11.2	[22]
11	$_{78}$Pt	L_{η}	9.975	0.163	[22]
12a	$_{78}$Pt	$L_{\beta 6}$	10.840	0.160	[22]
12b	$_{78}$Pt	$L_{\beta 4}$	10.854	0.083	[22]
12c	$_{78}$Pt	$L_{\beta 1}$	11.071	7.5	[22]
12d	$_{78}$Pt	$L_{\beta 3}$	11.235	0.109	[22]
12e	$_{78}$Pt	$L_{\beta 2,15}$	11.242	2.69	[22]
12f/13a	$_{78}$Pt	$L_{\beta 5}$	11.562	0.222	[22]
13b	$^{237}_{93}$Np	L_{l}	11.871	0.00864	[20] [23]
14	$_{78}$Pt	$L_{\gamma 1}$	12.942	1.47	[22]
15a	$_{78}$Pt	$L_{\gamma 2}$	13.273	0.027	[22]
15b	$_{78}$Pt	$L_{\gamma 3}$	13.361	0.037	[22]
16a	$^{237}_{93}$Np	$L_{\alpha 2}$	13.761	0.0115	[20] [23]
16b	$^{237}_{93}$Np	$L_{\alpha 1}$	13.946	0.1188	[20] [23]
17	Unknown (1)				
18	$^{237}_{93}$Np	L_{η}	15.861	0.00369	[20] [23]
19	$^{237}_{93}$Np	$L_{\beta 6}$	16.109	0.00246	[20] [23]
20a	$^{237}_{93}$Np	$L_{\beta 15}$	16.79	0.0012	[23]
20b	$^{237}_{93}$Np	$L_{\beta 2}$	16.816	0.0259	[20] [23]
20c	$^{237}_{93}$Np	$L_{\beta 4}$	17.061	0.0176	[20] [23]

20d	$^{237}_{93}$Np	$L_{\beta 7}$	17.27	0.0020	[23]
21a	$^{237}_{93}$Np	$L_{\beta 5}$	17.505	0.00465	[20] [23]
21b	$^{237}_{93}$Np	$L_{\beta 1}$	17.751	0.1160	[20] [23]
21c	$^{237}_{93}$Np	$L_{\beta 3}$	17.992	0.01222	[20] [23]
22a	$^{237}_{93}$Np	$L_{\beta 10}$	18.58	0.00075	[23]
22b	$^{237}_{93}$Np	$L_{\beta 9}$	18.76	0.00108	[23]
23	$^{237}_{93}$Np	$L_{\gamma 5}$	20.10	0.00121	[20] [23]
24a	$^{237}_{93}$Np	$L_{\gamma 1}$	20.784	1.39	[20]
24b	$^{237}_{93}$Np	$L_{\gamma 2}$	21.099	0.65	[20]
25a	$^{237}_{93}$Np	$L_{\gamma 8}$	21.26	0.00452	[23]
25b	$^{237}_{93}$Np	$L_{\gamma 3}$	21.342	0.0047	[20] [23]
25c	$^{237}_{93}$Np	$L_{\gamma 6}$	21.491	0.0060	[20] [23]
26a	$^{237}_{93}$Np	$L_{\gamma 4}$	22.22	0.00197	[23]
26b	$^{237}_{93}$Np	$L_{\gamma 13}$	22.38	0.00058	[23]
27a	$_{50}$Sn	$K_{\alpha 2}$	25.044	24.7	[22]
27b	$_{50}$Sn	$K_{\alpha 1}$	25.271	45.7	[22]
28	$^{237}_{93}$Np	Gamma (1)	26.345	2.40	[20]
29a	$_{50}$Sn	$K_{\beta 3}$	28.444	4.15	[22]
29b	$_{50}$Sn	$K_{\beta 1}$	28.486	7.99	[22]
30	$_{56}$Ba	$K_{\alpha 2}$	31.817	25.6	[22]
31a	$^{237}_{93}$Np	Gamma (2)	32.183	0.0174	[20]
31b	$_{56}$Ba	$K_{\alpha 1}$	32.194	46.7	[22]
32	$^{237}_{93}$Np	Gamma (3)	33.196	0.126	[20]
33	Unknown (2)				
34a	$_{56}$Ba	$K_{\beta 3}$	36.304	4.47	[22]
34b	$_{56}$Ba	$K_{\beta 1}$	36.378	8.63	[22]
35	$_{56}$Ba	$K_{\beta 2}$	37.255	2.73	[22]
36	$^{237}_{93}$Np	Gamma (4)	43.423	0.073	[20]
33	Unknown (3)				
37b	$^{237}_{93}$Np	Gamma (5)	59.541	35.9	[20]

Table 4.1: Nomenclature of all relevant photons with their energies and relative intensities

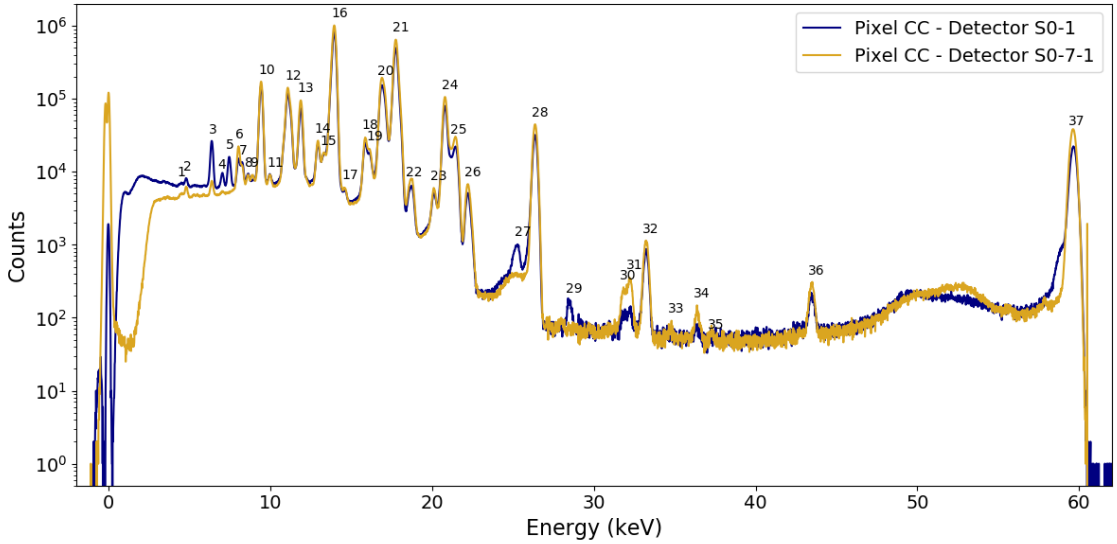

Figure 4.1: **Numerated Spectrum.** Numeration of all peaks of the long time $^{241}_{95}$Am spectrum considering the measurement from January 2019 and July 2020. One can see that some peaks disappear within the new spectrum. These peaks are Zn, Ni and Sn fluorescence lines. They probably arise because the previous detector generation (S0-1) was soldered to the holding structure in contrast to the new one.

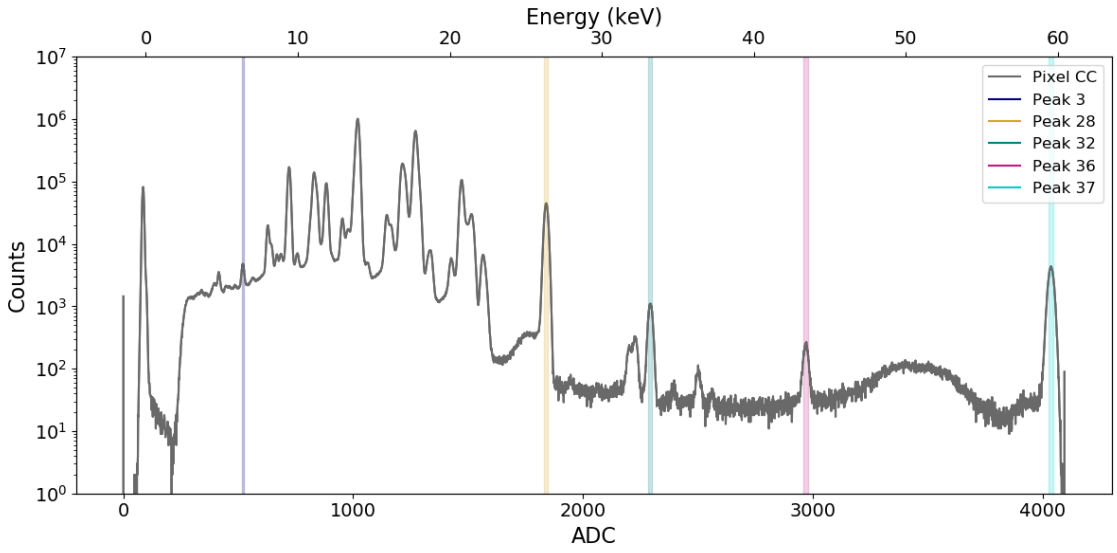

Figure 4.2: **Calibration-peak selection 1.** For selection one all big single peaks, which are clearly separated from any other peak were chosen.

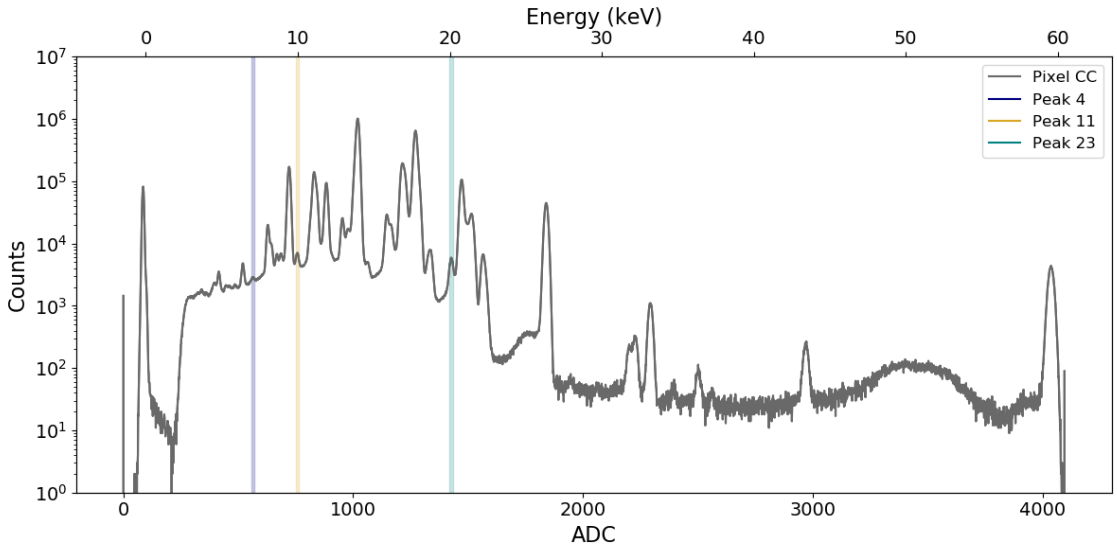

Figure 4.3: **Calibration-peak selection 2.** Selection two consists of either small single peaks or single peaks close to other peaks.

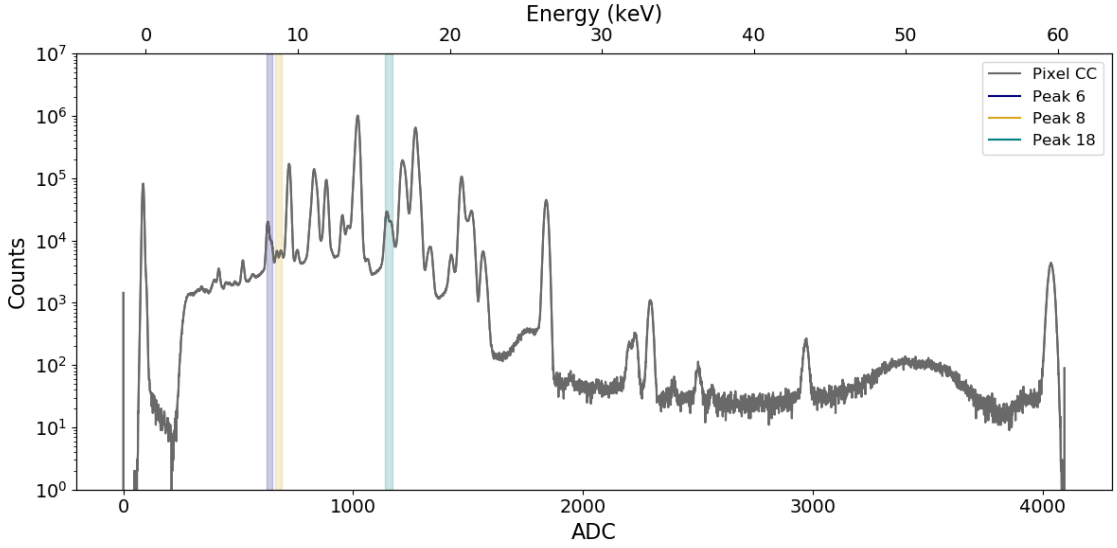

Figure 4.4: **Calibration-peak selection 3.** Category three consists of visually distinguishable double peaks.

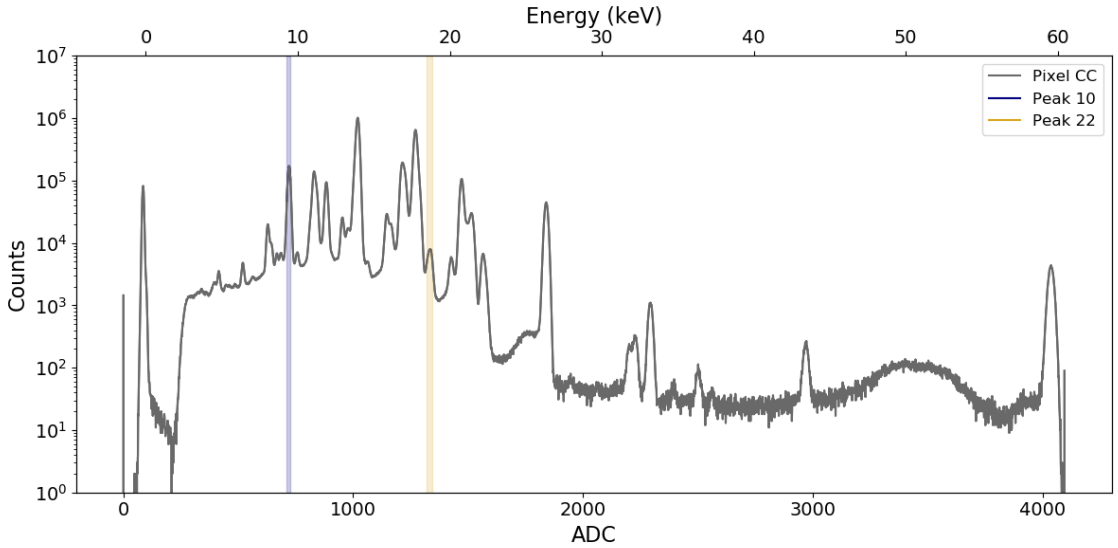

Figure 4.5: **Calibration-peak selection 4.** Category three are visually non-distinguishable double peaks fitted by a reduced Gaussian model as described in section 3.2.

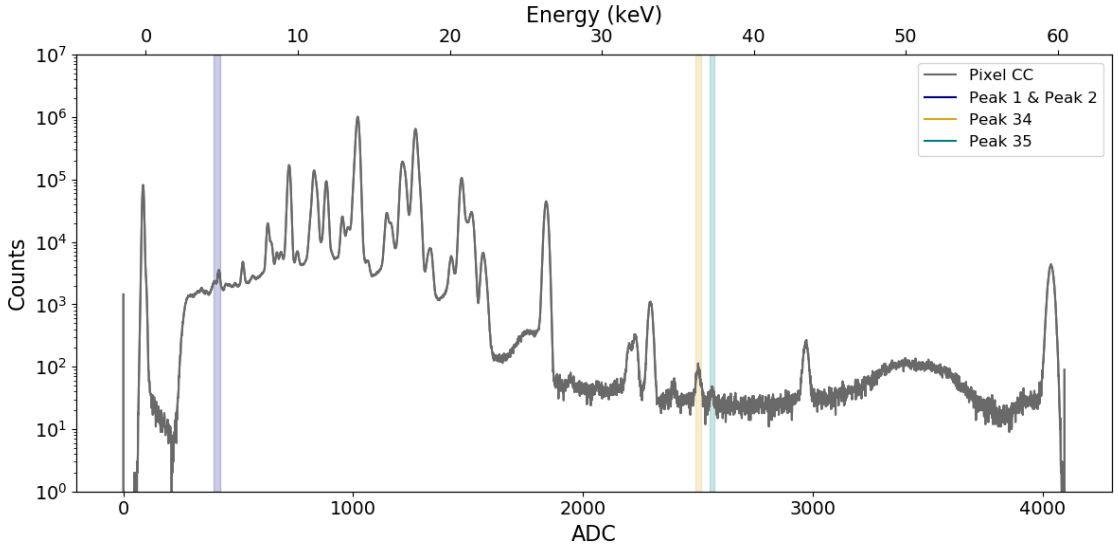

Figure 4.6: **Calibration-peak selection 5.** Barium and titan are treated specially in selection five, as their origin is still unexplained and they are situated in an area with major background.

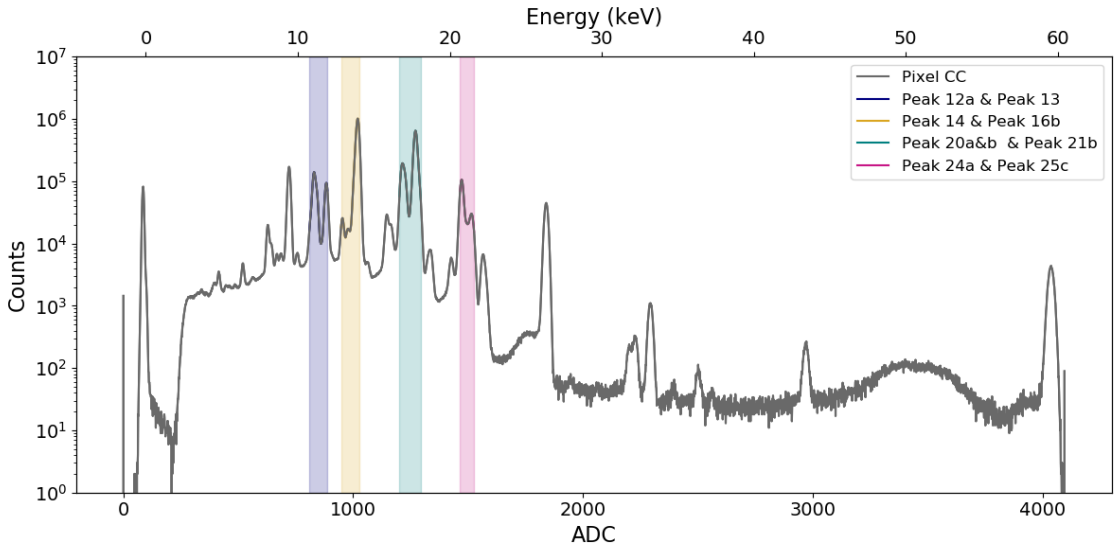

Figure 4.7: **Calibration-peak selection 6.** For peaks that consist of multiple peaks, selection six considers the peaks with the biggest intensity.

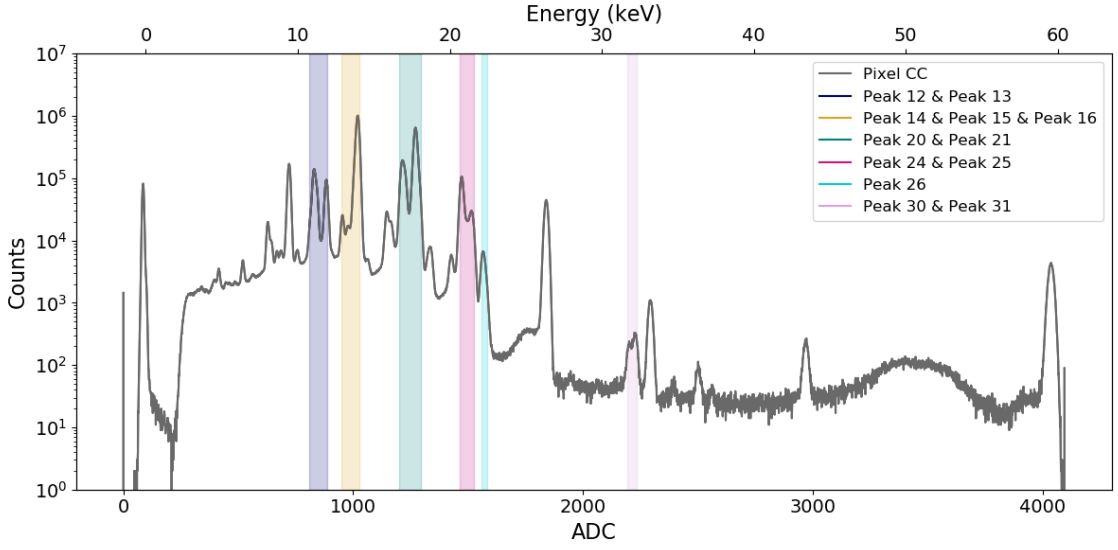

Figure 4.8: **Calibration-peak selection 7.** In category seven all remaining peaks are compiled.

List of Figures

1.1 Standard Model of elementary particles 6
1.2 KATRIN experimental setup 8
1.3 Neutrino mass signature in the tritium β-decay spectrum 9
1.4 Sterile neutrino signature in the tritium β-decay spectrum 10
1.5 TRISTAN detector design 12

2.1 SDD working scheme 14
2.2 Detector board with the seven pixel prototype detector 15
2.3 Pixel map 16
2.4 Experimental setup 17
2.5 Exemplary waveform 17
2.6 Energy peaking time sweep for different temperatures 18
2.7 Fast filter threshold sweep at 25 °C25°C 19

3.1 Am-241 spectrum of the central pixel 22
3.2 Exemplary Gaussian fit 24
3.3 Peak selection for a rough pre-calibration 25
3.4 Pre-calibration curve with estimation of the absolute calibration error . . . 27
3.5 Fano-plot based on the pre-calibration peaks 28
3.6 Identified charge sharing events between the central pixel with every adjacent pixel for a time window of 125 ns 29
3.7 Comparison of the spectrum with and without charge sharing events 30
3.8 Energy calibration results for different fitting ranges 32
3.9 Energy calibration results for different amounts of pre-selected peaks 33
3.10 Energy calibration and error estimation with selection one. 35
3.11 Long time stability investigation 36

4.1 Numerated Spectrum 43
4.2 Calibration-peak selection 1 43
4.3 Calibration-peak selection 2 44

4.4 Calibration-peak selection 3 44
4.5 Calibration-peak selection 4 45
4.6 Calibration-peak selection 5 45
4.7 Calibration-peak selection 6 46
4.8 Calibration-peak selection 7 46

Bibliography

[1] K. Urban. "Application of a TRISTAN Silicon Drift Detector as Forward Beam Monitor in KATRIN". Master Thesis. Technical University of Munich, 2019.

[2] S. N. Gninenko; D. S. Gorbunov and M. E. Shaposhnikov. "Search for GeV-scale sterile neutrinos responsible for active neutrino oscillations and baryon asymmetry of the Universe". In: *Advances in High Energy Physics* 2012.718259 (Dec. 2012). DOI: 10.1155/2012/718259.

[3] M. Cribier et al. "Results of the whole GALLEX experiment". In: *Nuclear Physics B - Proceedings Supplements* 70 (1–3 Jan. 1999), pp. 284–291. DOI: 10.1016/S0920-5632(98)00438-1.

[4] N. Barros et al. "Final results from SNO". In: *Nuclear Physics B - Proceedings Supplements* 237-238 (May 2013), pp. 107–110. DOI: 10.1016/j.nuclphysbps.2013.04.069.

[5] C. Giunti. "Theory of Neutrino Oscillation". In: *Particle Physics in Laboratory, Space and Universe* (2005), pp. 35–44. DOI: 10.1142/9789812702074_0005.

[6] M. Tanabashi et al. "Review of Particle Physics". In: *Physical Review D* 98.030001 (Aug. 2018). DOI: 10.1103/PhysRevD.98.030001.

[7] S. Mertens et al. "Sensitivity of next-generation tritium beta-decay experiments for keV-scale sterile neutrinos". In: *Journal of Cosmology and Astroparticle Physics* 2015 (Feb. 2015). DOI: 10.1088/1475-7516/2015/02/020.

[8] R. N. Mohapatra and G. Senjanović. "Neutrino Mass and Spontaneous Parity Nonconservation". In: *Physical Review Letters* 44.912 (Apr. 1980). DOI: 10.1103/PhysRevLett.44.912.

[9] G. Mention et al. "Reactor antineutrino anomaly". In: *Physical Review D* 83.073006 (Apr. 2011). DOI: 10.1103/PhysRevD.83.073006.

[10] S. Mertens et al. "A novel detector system for KATRIN to search for keV-scale sterile neutrinos". In: *Journal of Physics G: Nuclear and Particle Physics* 46.6 (May 2019). DOI: 10.1088/1361-6471/ab12fe.

[11] KATRIN Collaboration. *Katrin design report 2004*. Technical report. Forschungszentrum Karlsruhe, 2005. URL: http://bibliothek.fzk.de/zb/berichte/FZKA7090.pdf.

[12] D. B. Siegmann. "Investigation of the Detector Response to Electrons of the TRISTAN Prototype Detectors". Master thesis. Technical University of Munich, 2019.

[13] M. Descher. "High rate systematic effects for keV sterile neutrino searches at KATRIN". Master Thesis. Institute of Experimental Particle Physics, 2019.

[14] M. Aker et al. “Improved Upper Limit on the Neutrino Mass from a Direct Kinematic Method by KATRIN”. In: *Physical Review Letters* 123.221802 (Nov. 2019). DOI: 10.1103/PhysRevLett.123.221802.

[15] M. N. Mazziotta. “Electron–hole pair creation energy and Fano factor temperature dependence in silicon”. In: *Nuclear Instruments and Methods in Physics Research Section A* 584 (2-3 Jan. 2008), pp. 436–439. DOI: 10.1016/j.nima.2007.10.043.

[16] Oxford Instruments. The Business of Science., ed. *Silicon Drift Detectors Explained.* 2012.

[17] X. Pawlowski. “Characterization of the TRISTAN Silicon Drift Detectors with Krypton Conversion Electrons”. Bachelor Thesis. Technical University of Munich, 2018.

[18] T. B. Brunst. “First generation prototype detectors for the TRISTAN project”. Dissertation. Technical University of Munich, 2020.

[19] C. Bruch. “Investigation of the noise performance of silicon drift detectors for the TRISTAN project”. Bachelor Thesis. Technical University of Munich, 2020.

[20] S.Y.F. Chu; L.P. Ekström and R.B. Firestone. *The Lund/LBNL Nuclear Data Search.* Feb. 1999. URL: http://nucleardata.nuclear.lu.se/toi/index.asp.

[21] C. Forstner. “Pulse Shape Analysis with the TRISTAN Silicon Drift Detector”. Bachelor Thesis. Technical University of Munich, 2020.

[22] A. Thompson et al. *X-Ray Data Booklet. Center for X-ray Optics and Advanced Light Source.* 2009. URL: https://xdb.lbl.gov/.

[23] M.C. Lépy; B . Duchemin and J. Morel. “Comparison of experimental and theoretical L X - ray emission probabilities of ^{241}Am, ^{239}Pu and ^{240}Pu”. In: *Nuclear Instruments and Methods in Physics Research Section A* 353 (1–3 Dec. 1994), pp. 10–15. DOI: 10.1016/0168-9002(94)91591-1.